CHALMERS
UNIVERSITY OF TECHNOLOGY

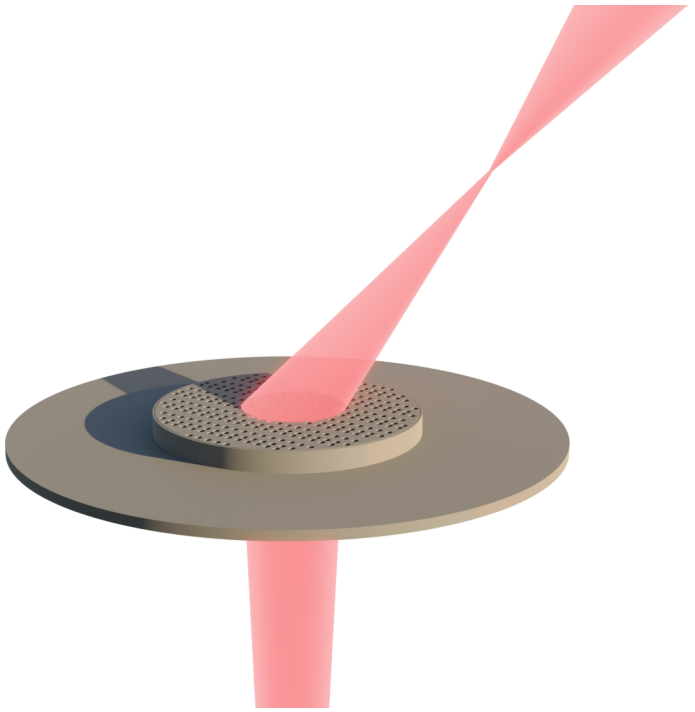

Large-angle deflection lens using supercell metasurfaces

A focusing metalens, for monolithical VCSEL integration, utilizing nano-holes to circumvent aspect ratio dependent etching

Master's thesis in Nanotechnology

KERSTIN VAHLIN

DEPARTMENT OF MICROTECHNOLOGY AND NANOSCIENCE
CHALMERS UNIVERSITY OF TECHNOLOGY
Gothenburg, Sweden 2024
www.chalmers.se

Master's thesis 2024

Large-angle deflection lens using supercell metasurfaces

A focusing metalens, for monolithical VCSEL integration, utilizing nano-holes to circumvent aspect ratio dependent etching

KERSTIN VAHLIN

CHALMERS
UNIVERSITY OF TECHNOLOGY

Department of Microtechnology and Nanoscience
Photonics laboratory
Chalmers University of Technology
Gothenburg, Sweden 2024

Large-angle deflection lens using supercell metasurfaces
A focusing metalens, for monolithical VCSEL integration, utilizing nano-holes to circumvent aspect ratio dependent etching
KERSTIN VAHLIN

Supervisor: Erik Strandberg, Department of Microtechnology and Nanoscience, Photonics laboratory
Examiner: Åsa Haglund, Department of Microtechnology and Nanoscience, Photonics laboratory

Master's Thesis 2024
Department of Microtechnology and Nanoscience
Photonics laboratory
Chalmers University of Technology
SE-412 96 Gothenburg
Telephone +46 31 772 1000

Cover: A metasurface consisting of nano-holes arranged to deflect and focus light. The metasurface can be monolithically integrated with a VCSEL.

Typeset in LaTeX
Printed by Chalmers Reproservice
Gothenburg, Sweden 2024

Large-angle deflection lens using supercell metasurfaces
A focusing metalens, for monolithical VCSEL integration, utilizing nano-holes to circumvent aspect ratio dependent etching
KERSTIN VAHLIN
Department of Microtechnology and Nanoscience
Photonics laboratory
Chalmers University of Technology

Abstract

A metasurface is an ultra-thin flat optical component, containing nanostructures that scatter light. Due to the planar structure it can be monolithically integrated with a vertical cavity surface-emitting laser (VCSEL), which removes alignment issues. With metasurfaces, full control of the wavefront is possible and hence a light beam can be shaped in almost anyway. For instance focusing metalenses, lenses that deflect light or vortex generators can be made. In many applications, for example in bio-photonics, it is desirable to have a lens with high numerical aperture, which entails deflection of light with large angels. The conventional way of designing a metasurface is to use phase mapping, however that approach has a fundamental limitation when it comes to creating steep angles. Therefor another type of metasurface based on diffracting elements have been implemented in this project. More specifically, these metasurfaces are made in GaAs to enable integration with GaAs VCSELs and the diffracting elements (supercells) are structured by nano-holes to get the desired light shape and circumvent the issue of aspect ratio dependent etching (ARDE).

The metasurfaces were first simulated in COMSOL, then fabricated using electron-beam lithography and dry etching, and finally characterized. Metalenses utilizing supercells that deflect light up to 85° have been achieved. The lenses deflect with the desired angle and show a focusing effect. However the focus of the lenses is not as tight as desired and calls for further investigation.

Keywords: metasurface, VCSEL, COMSOL Multiphysics

Acknowledgements

Firs of all I'd like to thank my examiner Åsa Haglund for the opportunity to do my Master's thesis at the Photonics laboratory. I'd also like to show great appreciation to my supervisor, Erik Strandberg, for excellent help and guidance and for being available for questions at all times. A thank you to Philippe Tassin for giving me access to the cluster VERA to run simulations. Thanks to Albin Jonasson Svärdsby and Timo Gahlmann for helping me set up the script to run simulations on VERA. Thanks to Willem de Wilde for computational hours and COMSOL advice. Lastly, I'd like to thank the clean room staff at Chalmers, especially Niclas Lindvall who helped me with the software for the e-beam machine.

Kerstin Vahlin, Gothenburg, June 2024

Contents

List of Figures

List of Acronyms

Below is the list of acronyms that have been used in this thesis, listed in alphabetical order:

ARDE	Aspect ratio dependent etching
DBR	Distributed Bragg reflector
EEL	Edge-emitting laser
LOC	Lab-on-a-chip
PML	Pefectly matched layer
VCSEL	Vertical-cavity surface-emitting laser

1
Introduction

Laser (Light Amplification by Stimulated Emission of Radiation) is a light source that utilizes stimulated emission to produce light. The stimulated emission creates a coherent, collimated beam with a narrow linewidth, which are all properties that are highly sought after in applications that require a precise light source. The semiconductor laser is one of the most important and used types of lasers, since it is low-cost, compact and power-efficient. This makes them suitable for applications like communication, in printers, DNA sequencing and measurement systems [1]. Semiconductor lasers take advantage of the bandgap between the conduction and valence band of the material to emit photons with a certain wavelength, and since there are many different semiconducting materials with different sized bandgaps, a span of wavelengths can be realized. To give two examples, the material system AlGaAs-GaAs is used for red to infra-red light and InGaN-AlGaN is used for green, blue and ultraviolet light.

As with any technology, there are many different kinds of semiconducor lasers. The two main types are the edge emitting laser (EEL), which as the name suggest emits light at the edge of the chip, and the vertical-cavity surface-emitting laser (VCSEL), which has been used in this project. A VCSEL emits the laser beam perpendicular to the top surface, in contrast to an EEL. This makes it possible to test the laser after fabrication at wafer level. In comparison, EELs can't be tested until individual lasers have been prepared by cleaving and mounting [1]. VCSELs have a wide range of applications; optical communication, face recognition and proximity sensors, to mention a few [2] [3]. Roughly described, a VCSEL consists of a vertical resonator in which quantum wells are placed that generate photons when injected carriers interact with photons [1]. VCSELs are inherently single longitudinal mode due to their short cavity length, which can be compared with the cavity of EELs that can be up to a few millimeters in length. The VCSELs' aperture decides the transverse mode distribution of the laser, and by making it small enough it is possible to make the VCSEL lase with one mode, also known as a single-mode device. However, the small aperture makes the VCSELs' emitted Gaussian beam divergent ($> 30°$ FWHM), which is a drawback when for instance coupling light into a fiber [4].

One of the recent advancements in nanophotonics is the use of thin metasurfaces to manipulate light, replacing the bulky refractive optical components, like lenses. A metasurface is a thin layer consisting of nanostructures which act as small optical antennas, scattering light. The planar structure of a metasurface makes it possible to monolithically integrate them on the backside of VCSELs. This integration

removes the issue of having to align external lenses and other optical components, which could benefit applications like fiber communication, printing and face recognition [3].

Another possible area of usage for the metasurface integrated VCSELs is as a part of a lab-on-a-chip (LOC) device. Several VCSELs with differently designed metasurfaces can be used for different purposes or together. Previous work has shown high-contrast microscopy using metasurface integrated VCSELs that can be a part of a LOC device [2]. Another opportunity would be to create an optical tweezer, which could then be integrated on a LOC device. In optical tweezing, a laser beam is focused to capture and move e.g. particles or biomolecules to study them. However, in order to achieve a well focused beam, a metasurface with high numerical aperture is needed which implies that the light needs to be deflected and focused with a large angle. As a first step towards optical tweezing, the goal of this thesis is to design and fabricate a metasurface that can focus light from a VCSEL at a high deflection angle.

The metasurfaces that are fabricated in this project are made in GaAs, since they are to be monolithically integrated with infra-red VCSELs using that material system. Creating a metasurface in only one material, for monolithic integration, gives rise to a fabrication issue, namely aspect ratio dependent etching (ARDE), which needs to be addressed. Very briefly, the etching depth of the material is dependent on the distances within the pattern of the metasurface, where narrow areas will be etched to a shallower depth than broad areas. This aspect ratio dependent etching can potentially be prevented by including an etch stop layer. However, when being integrated into the substrate of a VCSEL as is the goal here, this is not possible.

In this project metasurfaces have been simulated, fabricated and characterized. This thesis will start with some background about electromagnetic waves, lasers and optical tweezing, followed by theory about and different types of metasurfaces. After that the used simulation method is described together with the outcome. The fabrication process of the metasurfaces will presented. Finally a comparison between simulation and characterization of the fabricated metasurfaces will be made.

2
Light and Laser

In this section some important concepts of electromagnetic theory will be presented. This will be followed by background about lasers and semiconductor lasers. Finally, an introduction to optical tweezing and what to consider for the metasurface design, will be given.

2.1 Electromagnetic waves

Light are electromagnetic waves that are governed by Maxwell's equations. This section will state some equations and definitions that are useful in understanding propagation of light. In short, the electromagnetic waves are oscillations of electric and magnetic fields that arise from the acceleration of charged particles. In a homogeneous, isotropic and linear media the oscillations of the electric and magnetic field are perpendicular to each other. A wave is often represented as a complex function. However, the complex notation just simplifies the mathematics, to get the actual field, only the real part needs to be considered. Since the electric and magnetic fields are perpendicular it is sufficient to state one. The wave function of the electric field can be written as,

$$\vec{E}(\vec{r},t) = \vec{E}_0 e^{j(\omega t - \vec{k}\cdot\vec{r})}, \tag{2.1}$$

where $\vec{E_0} = E_x\hat{x} + E_y\hat{y} + E_z\hat{z}$ is the amplitude of the electric field, ω the angular frequency of the sine wave, $\vec{r} = x\hat{x} + y\hat{y} + z\hat{z}$ is a position in space and $\vec{k} = k_x\hat{x} + k_y\hat{y} + k_z\hat{z}$ is the wave vector. The wave vector represents the propagation direction of the wave and its magnitude is inversely related to the wavelength, λ,

$$\lambda = \frac{2\pi}{k}, \qquad k = |\vec{k}| = \sqrt{k_x^2 + k_y^2 + k_x^2} \tag{2.2}$$

The wave in Equation 2.1 is a plane wave, which means that the wave front is constant in a plane. It is also monochromatic, meaning that it only contains one frequency, and it is fully polarized, meaning that the electric field (or magnetic field) of the wave is confined in a single plane perpendicular to the propagation direction. However, any real beam is always a superposition of many plane waves, the plane wave is the basis for any beam, with different frequencies and the polarization can for instance be circular which implies that the polarization plane rotates around the propagation axis. In Figure 2.1, a graphic representation of a linearly polarized plane wave can be seen.

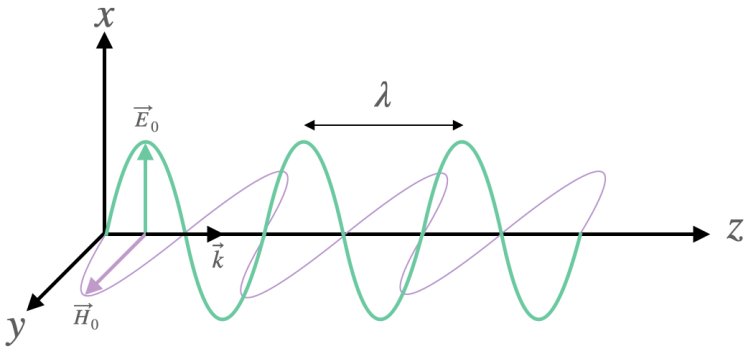

Figure 2.1: Graphic representation of a linearly polarized plane wave. The green sinus wave shows the electric field ($\vec{E}_0$) and the purple shows the magnetic field ($\vec{H}_0$). The wave vector, $\vec{k}$, marked with a black arrow, is in the propagation direction. The wavelength, λ, is also marked. The polarization plane is along the x-axis since the E-field is oscillating in that plane.

Electric and magnetic fields are described by Maxwell's equations, which by assuming no free charges or currents can be written as,

$$\begin{aligned} \nabla \times \vec{E} &= -\frac{\partial \vec{B}}{\partial t} \\ \nabla \times \vec{H} &= \frac{\partial \vec{D}}{\partial t} \\ \nabla \cdot \vec{D} &= 0 \\ \nabla \cdot \vec{B} &= 0, \end{aligned} \tag{2.3}$$

where $\vec{E}$ and $\vec{H}$ are the electric and magnetic field respectively. $\vec{D}$ and $\vec{B}$ are the electric displacement and magnetic induction, which represent the material response when an external field is applied, and can be expressed in terms of $\vec{E}$ and $\vec{H}$ as,

$$\begin{aligned} \vec{D} &= \varepsilon \vec{E} + \vec{P} \\ \vec{B} &= \mu \vec{H} + \vec{M} \approx \mu_0 \vec{H} + \vec{M} \end{aligned} \tag{2.4}$$

where $\varepsilon = \varepsilon_0 \varepsilon_r$ is the permittivity, ε_0 the vacuum permittivity and ε_r is the relative permittivity, $\mu = \mu_0 \mu_r$ the permeability with μ_0 and μ_r being the vacuum and relative permeability, respectively. However, the relative permeability is almost one for non-magnetic materials at optical frequencies, why only the vacuum permeability is often used. $\vec{P}$ and $\vec{M}$ are the electric and magnetic polarizations. Further, the refractive index (n), which describes the electromagnetic propagation in a material, is given by the relative permittivity and permeability, $n = \sqrt{\varepsilon_r \mu_r}$. From Maxwell's equations the wave equations can be derived, which are satisfied by the plane wave solutions, like the one in Equation 2.1. In this thesis Maxwell's equations are solved in simulations using the finite element method, which will be described further in the section about Simulations.

2.2 Laser

Laser, short for Light Amplification by Stimulated Emission of Radiation, is a technique that generates light via stimulated emission. This makes the emitted light close to monochromatic and coherent. A laser consists of an optical gain medium, which can produce light when the medium is supplied with energy, enough to create population inversion [1]. To induce lasing, the gain medium is surrounded by a resonator which provides optical feedback, by creating a standing wave at a desired wavelength. Population inversion and optical feedback are the two most important things to consider when creating a laser, and will be described further. There are many types of lasers and they are often named after what medium is used to generate light by population inversion. For instance, gas lasers, like the HeNe laser which is found in student labs, and free-electron lasers, that creates X-ray radiation for material science. The laser type used in this thesis is the semiconductor laser, which uses the band gap in a in semiconductor to create the needed population inversion. VCSELs are semiconductor lasers and will be discussed in the end of this section.

2.2.1 Population inversion

Population inversion is needed for optical gain and thus lasing and can be explained by considering a simple two-level quantum system, where electrons only can exist in two energy levels, E_1 and E_2. In each energy level the electron population densities are n_1 and n_2. In a photon-electron interaction in this system there are three possible transitions, involving photons, for electrons, see Figure 2.2. In the first one, absorption, an electron in the lower energy level is exited to the higher energy state by absorbing a photon. In the second transition, spontaneous emission, an electron in the higher energy level is deexcited to the lower energy level and emits a photon with the energy difference of the two energy levels. The phase of the emitted photon is random, why the outgoing beam is incoherent. In the last process, stimulated emission, the deexitation is a result of photon-electron interaction and again the energy difference is emitted as a photon, together with the incident photon. There are thus two photons created from one photon, which is the optical gain in lasers. The photons that are generated through stimulated emission have, unlike spontaneous emission, the same phase as the incoming photon which makes the light coherent. Further the direction and exact wavelength of the generated photon are also duplicated from the incident photon, which make the propagation direction and wavelength of the light the same.

The rate at which each process occurs can be described by the following equations,

$$\begin{aligned} R_{abs} &= B_{12} n_1 \rho_\gamma \\ R_{sp} &= A_{21} n_2 \\ R_{st} &= B_{21} n_2 \rho_\gamma, \end{aligned} \tag{2.5}$$

where B_{12}, A_{21} and B_{21} are the Einstein coefficients which describes the probability of absorption or emission, and ρ_γ is the photon density. In thermal equilibrium

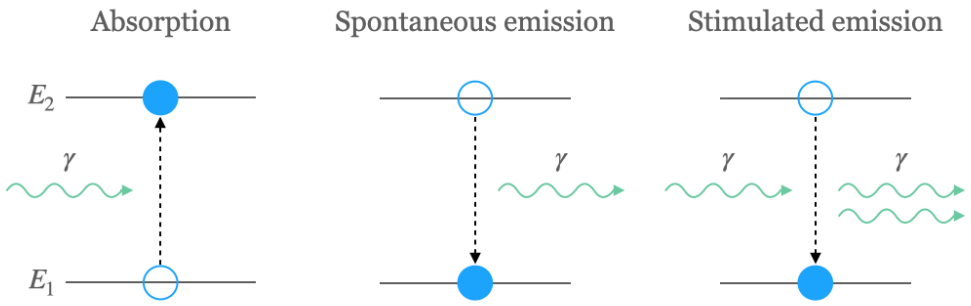

Figure 2.2: Three possible transitions for electrons interacting with photons, in a two level system. To the left, absorption, where an electron (blue dot) is excited from the first energy level (E_1) to the second level (E_2) by absorption of a photon (green arrow). In the middle, spontaneous emission, an electron is deexcited to the lower energy level which emits a photon. To the right, stimulated emission, where a deexcitation occurs after an electron-photon interaction resulting in coherent light emission which is what is used in lasers.

the lower energy state is more populated than the higher ($n_1 > n_2$) which makes the absorption rate, R_{abs}, higher than the emission rate, particularly the desired stimulated, R_{st}. To increase the rate of stimulated emission, the laser medium is pumped with energy which makes the population of the higher energy state increase. This is what is referred to as population inversion, when $n_2 > n_1$. However the population inversion does not only increase stimulated emission, but also spontaneous, R_{sp}, which in addition tends to dominate over stimulated emission since often $A_{21} > B_{21}$. Hence, a substantial part of the light is incoherent, which is what is used in light emitting diodes (LED). For a laser however, coherent light is desired so the stimulated emission needs to dominate over the spontaneous, which can be achieved by optical feedback.

2.2.2 Optical feedback

From Equation 2.5, it can be seen that the expression for the rate of stimulated emission is proportional to the photon density, ρ_γ. To get a high photon density the pumped medium is placed in a resonator, which creates an optical feedback loop for the mode of light from the stimulated emission. The most simple resonator is a Fabry-Pérot cavity with two plane mirrors (R_1 and R_2) at a distance L from each other, see Figure 2.3. Generated light from stimulated emission is reflected by the mirrors, making it propagate forward and backwards. With the correct dimensions of the cavity (L), the superposition of the back- and forward propagating waves, creates a standing wave. This makes the photons from the stimulated emission stay in the cavity, and in turn generate even more photons. This creates a self-oscillating system, which makes the photon density grow.

To create a standing wave, the electromagnetic field needs to reproduce itself in phase and amplitude after one round-trip in the cavity. This gives rise to a phase

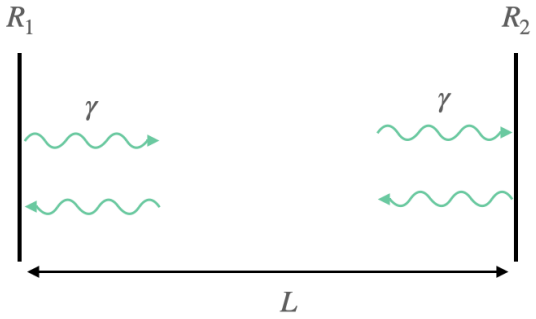

Figure 2.3: Fabry-Pérot cavity for optical feedback. The cavity is made of two plane mirrors (R_1 and R_2) which are placed a distance L from each other. The mirrors reflects the photons which creates standing waves, also known as optical feedback.

and an amplitude condition, in a Fabry-Pérot cavity. The phase condition is,

$$e^{-jk_0 n_{eff} 2L} = 1 \implies k_0 n_{eff} 2L = 2\pi m \implies \lambda_0 = \frac{2Ln_{eff}}{m} \tag{2.6}$$

where λ_0 is the resonance wavelength, L is the cavity length, n_{eff} is the effective refractive index of the mode and m is an integer. As can be seen from this condition, the length of the cavity and the refractive index of the pumped media decides the resonant wavelengths.

The second condition, the amplitude condition, describes the balance between the round-trip losses in the medium and mirrors, and the gain from the active region. From its expression, the material threshold gain is obtained,

$$\sqrt{R_1 R_2} e^{\Gamma(g-\alpha_i)L} = 1 \implies g_{th} = \frac{1}{\Gamma}\left(\alpha_i + \frac{1}{2L}\ln\frac{1}{R_1 R_2}\right), \tag{2.7}$$

where Γ is the optical confinement factor which is the fraction of the optical mode in the active region. g and g_{th} are the gain and threshold gain respectively and α_i is all the losses in media due to propagation. When the threshold gain is surpassed, one photon on average generates more than one photon after one round-trip in the cavity. This leads to the self-oscillation feedback that starts the lasing.

2.2.3 Semiconductor lasers and VCSELs

In a semiconducting laser, population inversion is established in a semiconductor material usually through current injection. The current injection excites electrons from the valance band, E_v, to the conduction band, E_c, creating population inversion. That means that the wavelength of the emitted photons is determined by the bandgap of the semiconducting material ($E_g = E_c - E_v$), see Figure 2.4. Since there exist a wide range of semiconductors with different bandgaps, lasers with different wavelength can be engineered. For instance, the material system AlGaAs-GaAs system is used for the wavelengths 750-850 nm and InGaN-AlGaN is used for wavelengths around 250-550 nm. The optical feedback is achieved by creating interfaces

between semiconducting materials with different refractive index which gives reflection. The main types of semiconducting lasers are the edge-emitting laser (EEL) and the vertical-cavity surface-emitting laser (VCSEL) which differs by the direction of emission. In this work VCSELs are used for integration with metasurfaces and will be explained further.

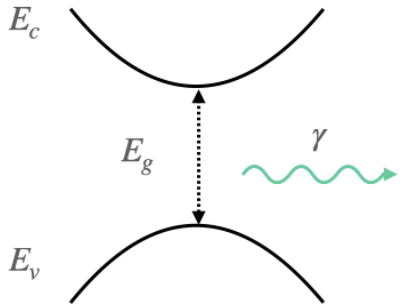

Figure 2.4: The valence band (E_v) and the conduction band (E_c), which makes up two significant energy levels in semiconductors. The energy difference between the bands is called the bandgap and is marked with E_g ($= E_c - E_v$). The wavelength of the emitted photon is set by the bandgap.

A vertical-cavity surface-emitting laser (VCSEL) is a semiconductor laser that emits a laser beam perpendicular to the top surface. VCSELs have high efficiency and are well compatible for wafer-scale production [2]. A great advantage with VCSELs, compared to EELs, is that they can be tested after fabrication at wafer level without mounting them. This can't be done with EELs, which have to be cleaved and mounted before testing [1]. VCSELs have a wide range of applications, like optical communication, face recognition and proximity sensors, to mention a few [2] [3].

In this project metasurfaces that can be integrated with VCSELs made of the material system AlGaAs/GaAs has been considered, which generates light at the wavelength $\lambda = 984$ nm with an output power of 1-5 mW. A VCSEL consists of a vertical resonator with quantum wells inside which generate photons when injected carriers interact with photons, see Figure 2.5 [1]. Each quantum well, which together make up the active region, contains a designed conduction and valence band, in which the population inversion can take place. Quantum wells are, compared to bulk material, reduced below the de Broglie wavelength in one dimension which makes the movement of particles in that direction restricted. This confines the carriers and creates a higher density of states at the band edge, which increases lasing efficiency and gives a higher gain. Since the volume of the quantum wells is very small, only a small current is needed to achieve population inversion, compared to bulk lasers. The quantum wells are designed to make the laser lase at the desired wavelengths, by varying the material composition of the layers to get different sized band gaps, see Figure 2.6. The resonator, which creates the optical feedback, is made of two distributed Bragg reflectors (DBRs), which can also be seen in Figure 2.5. A DBR is

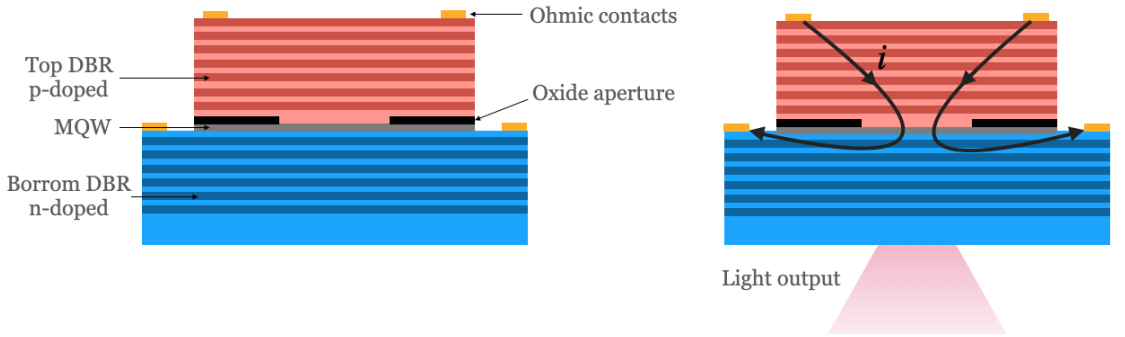

Figure 2.5: Sketch of a GaAs VCSEL. To the left the parts making up the VCSEL are marked; doped DBRs, multiple quantum wells (MQW), the oxide aperture and ohmic contacts for current injection. To the right, the path of the pumping current, i, and the light output can be seen.

formed by growing layers with different refractive index. Each layer causes the light to reflect, but also to refract. In addition, if the optical thickness of the layers are made to be a quarter of the wavelength, constructive interference is created between the reflected beams of the different layers. Assuming that the optical thickness of the layers are a quarter wavelength, the intensity of the reflectivity is given by,

$$R = \left(\frac{(n_{in}n_2)^{2N} - (n_{out}n_1)^{2N}}{(n_{in}n_2)^{2N} + (n_{out}n_1)^{2N}} \right), \tag{2.8}$$

where n_{in} and n_{out} are the refractive indices of the material before and after the DBR, n_1 and n_2 are the refractive indices of the layers in the DBR and N the number of layers. To make the VCSEL lase, the reflectivity of the DBRs has to be greater than 99%, due to the thin gain medium, see Equation 2.7. Moreover, one DBR has lower reflectivity than the other to allow for emission of the light created in the active region. In addition, the DBRs are doped, one is p-doped and the other is n-doped. This is to supply the quantum wells with free electrons and holes. The VCSEL also has contacts for current injection and an oxide aperture, which is seen in Figure 2.5. The aperture has two functionalities. The first is to confine the current laterally, to minimize losses to the rest of the structure and get carriers in the quantum wells. The other is to create a waveguide structure to make the VCSEL lase with one mode, making it a single-mode device. The emitted light from the VCSEL is a Gaussian beam that diverges which can make efficient coupling to for instance optical fibers, an issue [4]. Finally, the emitted light is also linearly polarized.

2.3 Optical tweezing

Optical tweezing is a method that focuses a laser beam in order to capture and move objects like molecules, atoms and nanoparticles. The development of this method was awarded the Nobel prize in 2018 and it has many applications in physics and biology. For instance it can be used in medicine to capture and study biomolecules

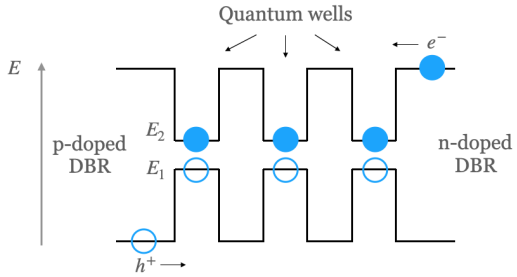

Figure 2.6: Multiple quantum wells, that makes up the active region of a VCSEL. Each quantum well well is injected with carries (e^- and h^+) which creates population inversion making it possible to achieve optical gain.

like molecular motors, DNA and bacteria [5]. Or in quantum optics to investigate single particle interaction with light.

To get a tightly focused laser beam, creating a trap, an objective lens with high numerical aperture (NA) is often used [5]. When light is scattered on a particle near the focus, it will deflect, which changes the momentum of light ($\vec{k}$). Due to conservation of momentum a force with opposite momentum will be exerted on the particle. The change of momentum depends on where on the particles' surface the light scatters and the intensity of light. Hence, the position of the particle relative to the beam affects the change of momentum and therefore the force on the particle. The intensity of a light beam varies in space, it has an intensity gradient. The intensity gradient of a Gaussian beam is characterized by the Gaussian function, meaning that the highest intensity is in the middle of the plane perpendicular to the propagation direction. If the particle is displaced from the center of a Gaussian beam, the force will be directed towards the center of the trap since the momentum change is greater for higher intensity than lower, making the resulting force pointing towards the high intensity center. For a particle in the center of the beam, the forces in the direction of the intensity gradient will be canceled out while the forward force will be kept. This makes the particle stay in the middle of, but slightly downstream, the light beam. The force affecting the particle is often, for convenience, decomposed into two forces: a scattering force in the light propagation direction and a gradient force in the direction of the gradient. With an intensity gradient perpendicular to the beams' propagation direction a two dimensional optical trap can be made. Using a well focused laser, a longitudinal intensity gradient in the propagation direction can be established, creating a three dimensional optical trap.

A theoretical explanation of the forces in an optical trap needs to be treated in three different cases, depending on the particle size (radius, r) relative to the wavelength (λ) [5] [6]. The first case is when the particle size is much larger than the wavelength ($r \gg \lambda$). The conditions for Mie scattering are filled and ray optics can be used. Individual rays from the laser beam are refracted by the particle, which changes the momentum carried by light. According to Newton's third law, an equal and opposite momentum change is transmitted to the particle. The magnitude of the

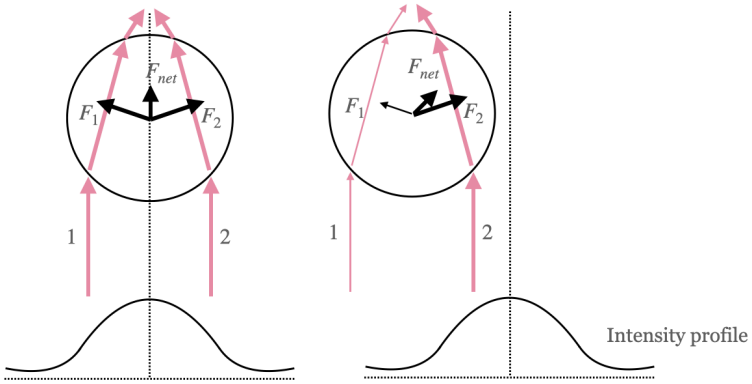

Figure 2.7: Forces acting on a particle (circle) in the Ray optics view. On the left hand side, when the particle is in the middle of the beam and on the right hand side when the particle is displaced with respect to the beam.

force acting on the particle due to the change of momentum is proportional to the light intensity. The direction of the force is the same (attractive) as the intensity gradient if the refractive index of the particle is greater than the surrounding, and the opposite direction for lower refractive index. In the ray picture, the rays in the middle of the beam mainly contributes to the scattering force while the outer rays with higher angles constitutes the gradient force, see Figure 2.7.

When the particle is much smaller then the wavelength ($r \ll \lambda$), the second case needs to be considered, where Rayleigh scattering is applicable. This type of scattering originates from the trapped particles' polarizability. Since the electric field of light is oscillating, charges in the particle will move with the same frequency, making it a point dipole. A single point charge in an electromagnetic field will experience a force, the Lorentz force,

$$\vec{F} = q(\vec{E} + \vec{v} \times \vec{B}),$$

where q is the charge of the particle, $\vec{v}$ is the velocity of the particle, $\vec{E}$ and $\vec{B}$ are the electric and magnetic field. Describing a dipole as a sum of two single point charges with opposite charge, the following expressions for the scattering and gradient forces can be obtained.

$$\begin{aligned} \vec{F}_{scatt} &= \frac{I_0 n}{c} \frac{128\pi^5 r^6}{3\lambda^4} \left(\frac{m^2 - 1}{m^2 + 2} \right)^2 \\ \vec{F}_{grad} &= \frac{2\pi n r^3}{c} \left(\frac{m^2 - 1}{m^2 + 2} \right)^2 \nabla I_0, \end{aligned} \tag{2.9}$$

were I_0 is the light intensity, n the refractive index of the medium surrounding the particle, c is speed of light in vacuum, r is the particle radius, λ the light wavelength and m is the ratio of refractive index between the particle and the surrounding medium. Note that these equations are for spherical particles. From these equations

it can be seen that the scattering force is proportional to the intensity, while the gradient force is proportional to the intensity gradient.

Lastly, when the particle size is approximately the same as the wavelength ($r \approx \lambda$) neither Mie or Rayleigh scattering can be used. Instead full electromagnetic theory, meaning solving Maxwell's equations with appropriate boundary conditions, needs to be considered. Optical tweezing of particles in this range are hard to model. However, experiments show that there is no major difference from the behaviour of Rayleigh particles [6].

One possible area of usage for metasurface integrated VCSELs is to create an optical tweezer, for example as a part of a LOC device. It has previously been shown that VCSELs, using external objectives, can be used for optical tweezing [7] [8] [9] [10] [11]. It has also been shown that metasurfaces can be used for optical trapping, but using another metasurface material and not a VCSEL as the light source [12]. An optical tweezer that is based on a metasurface integrated VCSEL, has to the authors' knowledge and to this date not been demonstrated. As mentioned previously, a high numerical aperture is required for trapping. That in turn means that the metasurface needs to be able to deflect light with a large angle. This has been the starting point for the design of the metasurfaces in this project.

3
Metasurface

This chapter gives a background to the concept of metasurfaces, different examples of it and what type of metasurfaces will be fabricated in this project.

3.1 Deflection of light

Historically, and still today, lenses have been used to bend and focus light into desired directions and focal points. Traditional lenses, also known as refractive optics, are based on gradual phase changes that are accumulated as the light propagates through it. However, only phase shifts between 0 and 2π are of importance, everything that is just and integer multiplied with 2π will just add a constant since light are waves with a phase that is repeated in cycles of 2π. One of the recent advancements in nanophotonics is the use of thin metasurfaces to bend the light, replacing the bulky refractive optical components. A metasurface is a thin layer consisting of nanostructures which act as small optical antennas, scattering light. The antennas are arranged in arrays and can for instance be meta-atoms or small apertures [13]. Meta-atoms are small resonators which depending on their geometry (e.g. shape, size and orientation), creates different geometric resonances which, together with already existing resonances (e.g. electron resonances) of the material, affects the effective refractive index. The change of effective refractive index gives rise to phase delays of the scattered light. Consequently, the need of light propagation to achieve phase change is reduced and the metasurface can be made very thin [4]. The planar structure also makes it possible to monolithically integrate them on the backside of VCSELs. The integration removes the issue of having to align external lenses and other optical components.

Metasurfaces are designed in such way that phase shifts, ranging from 0 to 2π, can be made over sub-wavelength spatial distances, which gives full control of the wave front [14]. This is realized by designing a two dimensional array of meta-atoms that are located on the metasurface. Each meta-atom adds a phase delay to the passing light, creating a phase gradient over the metasurface. With the phase gradient in mind, a generalization of Snell's law can be expressed,

$$n_t \sin(\theta_t) - n_i \sin(\theta_i) = \frac{\lambda_0}{2\pi} \frac{d\Phi}{dx},$$

where θ_i and θ_t are the incident and transmitted angles respectively, n_i and n_t the refractive indices of the two media, λ_0 is the vacuum wavelength and $\frac{d\Phi}{dx}$ the phase

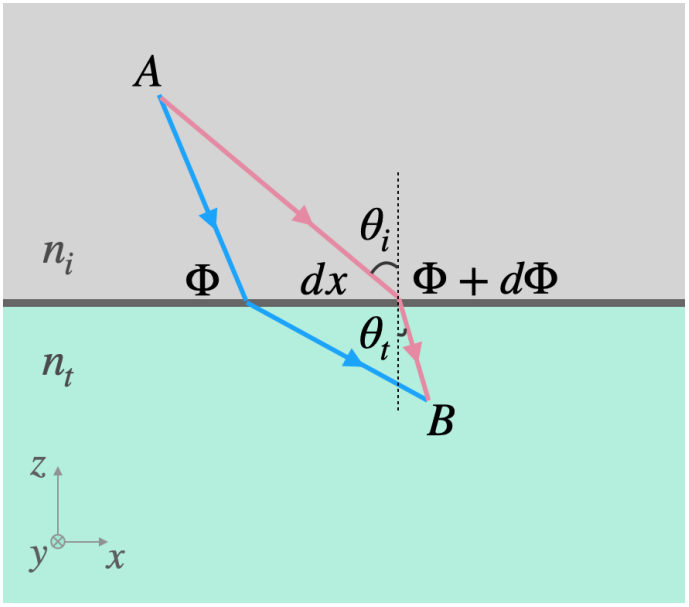

Figure 3.1: Visualization of Snell's generalized law. Light propagates from point A in one media (refractive index n_i) to point B in another media (n_t). This can be done by taking the blue or the pink path, which are both infinitesimally close to the actual path (governed by Fermat's principle), which gives a phase difference of zero between them. At the interface of the two media is a structure (dark grey) which introduces a phase shift in the path of light as a function of the position on the interface (x). Φ is added to the blue path and $\Phi + d\Phi$ is added to the pink path. θ_i and θ_t is the angle of incidence and transmission, respectively.

gradient. The equation states that the transmitted beam can have any shape, given a suitable phase gradient [14]. A visualization of the parts in the equation can be seen in Figure 3.1.

With metasurfaces it is possible to get the same effects as with lenses, since full control of the wavefront can be achieved. For instance a collimating lens or a focusing lens can be created. When it comes to lenses, the numerical aperture (NA) is an important number which measures how much light that can be gathered in one point. NA is defined as,

$$\mathrm{NA} = n \sin \theta,$$

where n is the refractive index surrounding the lens and θ is the half angle of the cone of light that can enter the lens, see Figure 3.2. In the same figure the focal length f, which is the distance to the focus point and the lens diameter L, is also marked.

There are different types of metasurfaces which uses different design approaches to modulate the phase. One example is dynamic phase (also propagation phase or effective index of wave guides) metasurfaces, where the size of the meta-atom in a cell of the array determines the cell's effective refractive index. By altering the size, the

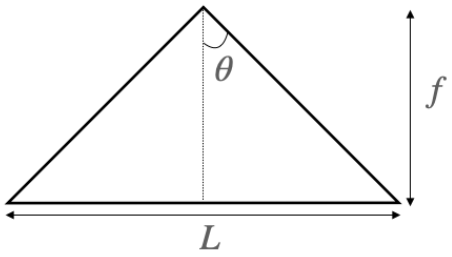

Figure 3.2: Half angle, θ, defining numerical aperture, focal length f and lens diameter L.

effective refractive index is changed, which in turn changes the phase delay. Another type is the geometric phase (also Pancharatnam Berry phase) metasurface. In this method a birefringent meta-atom is placed in each cell and by changing the orientation of the meta-atom the phase delay can be controlled. The last type is called resonant metasurfaces. The idea is to operate around the resonance frequency, which is a sum of the materials' electron resonances and the geometric resonances from the meta-atoms. All the mentioned methods are based on phase mapping, meaning that each cell produces the desired phase delay. In this project a diffraction based metasurface, which is a subcategory to the dynamic phase metasurface, has been used and will be explained further.

3.2 Dynamic phase metasurface

The conventional way to design a metasurface is to utilize phase mapping. A phase map shows a continuous function of what phase delay, which is mimicing the refractive index counterpart, that needs to be added in each spatial point of the metasurface to get, for instance, a collimating lens, such a phase map can be seen in Figure 3.3a. To realize the phase map on a physical metasurface, it is discretized into periods, see Figure 3.3b. Note that the lattice period is smaller than the wavelength in the substrate, since that only allows for coupling into the zeroth diffraction order,

$$P^2 < \left(\frac{\lambda_0}{n}\right)^2, \tag{3.1}$$

where P is the length of the period and n is the refractive index of the medium. The equation is derived and explained further in the next chapter about diffractive based metasurfaces. Within each period, or cell, a certain phase delay, according to the discretized phase map, should be added, which is done by placing a meta-atom that corresponds to the correct phase delay. In the dynamic phase approach, this is accomplished by changing the size of the meta-atom in the period. This will change the effective refractive index of the cell and hence the phase delay. A meta-atom can in this case be a nano-pillar, as can be seen in zoomed in part of Figure 3.3b, that

adds different phase delays depending on the radius. The pillars can be made in various materials and on various substrates, but are usually etched into a high-contrast dielectric material, since having a high refractive index contrast localizes more of the field inside the pillar, which gives a stronger dependency between the geometry of the pillar and the phase delay. Other shapes like squares or rectangles, are also possible, however utilizing a rotational symmetric meta-atom the polarization state of the beam will not be changed.

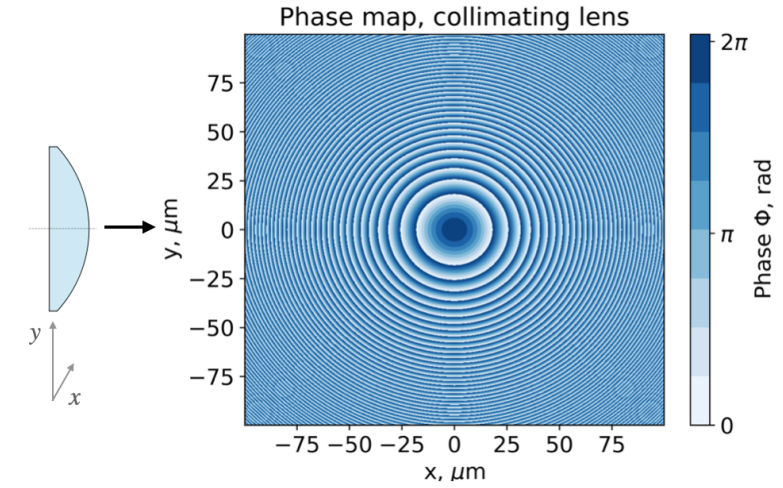

(a)

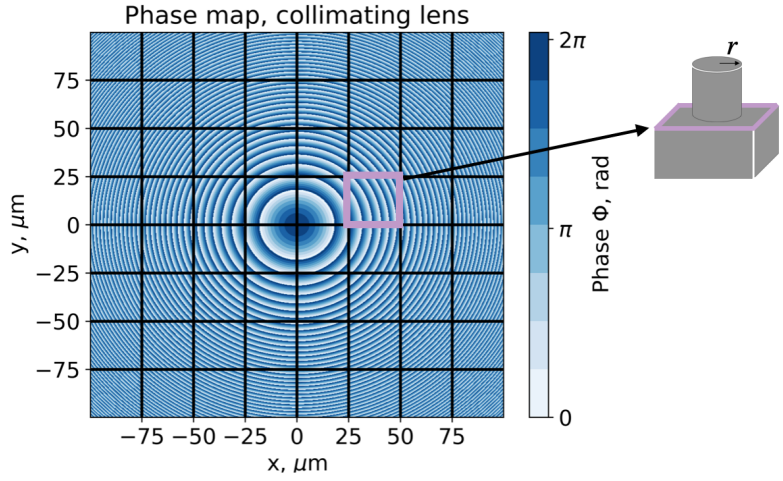

(b)

Figure 3.3: (a) Phase map of a collimating lens which shows what phase delay that needs to be added in each continuous point of a surface. (b) shows the same phase map, but with a grid that represents the discretization of the phase map. In each period of the grid a meta-atom that corresponds to the desired phase delay should be placed. To the right an example of a meta-atom containing a pillar can be seen. The desired phase-delay can be achieved by varying the radius of the pillar.

The phase mapping approach works well for smaller angles, but for larger angles most of the energy is dissipated into the structure, making the efficiency low [15] [16]. Larger angles requires a very steep phase gradient which calls for a discretization that can be hard to realize in fabrication.

3.3 Diffraction based metasurface

A variant of the dynamic phase metasurface is to use diffractive elements which, as the name suggests, builds on diffraction of light. As discussed, a problem with the phase mapping approach is that it is hard to achieve large deflection angles with good efficiency. With diffraction based metasurfaces, on the other hand, large deflection angles can be achieved with high efficiency. This can be circumvented by using diffractive meta-atoms. A periodic pattern is designed in such way that higher diffraction orders are opened, which in contrast to the zeroth order have deflection angles with respect to the normal. One period, or cell, consists of various amounts of structures, like nano-pillars, with a geometry designed to favor one desired diffraction order and cancel out the unwanted ones. This is often referred to as a supercell metasurface, since one periodicity contains several scatterers, or a metagrating in two dimensions. For instance, if the period of the pattern is chosen to be diffractive for the first order, that means that the orders T_0, T_1 and T_{-1} are transmitted, as can be seen in Figure 3.4. However, if the wanted bending direction corresponds to transmission of the first positive order, T_1, then the design within a period needs to be made in such a way that the scattering pattern redistributes the energy into that bending direction, see inset of Figure 3.4. Note that in the phase mapping approach one needs to consider the diffraction as well to be sure that no higher diffraction orders are opened, since it leads to unwanted energy leakage. Possible diffraction orders can be derived by looking at the diffractive grating in Figure 3.5. The derivation will be done in one dimension for clarity, but additional dimensions can be calculated in the same way. Starting by separating the components of the wave vector of the incoming ($\vec{k_i}$), realizing that the grating will add momentum only in the plane of the grating, and then expressing the momentum of the transmitted ($\vec{k_t}$) and reflected ($\vec{k_r}$) light,

$$\begin{aligned} \vec{k_i} &= k_{i,z}\hat{z} + k_{i,x}\hat{x} \\ \vec{k_t} &= \vec{k_i} + \vec{G} = k_{i,z}\hat{z} + k_{i,x}\hat{x} + G\hat{x} \\ \vec{k_r} &= \vec{k_i} + \vec{G} = k_{i,z}\hat{z} + k_{i,x}\hat{x} + G\hat{x}, \end{aligned} \tag{3.2}$$

where $\vec{G} = \frac{i2\pi}{P}\hat{x}$ is the reciprocal lattice vector and $G = |\vec{G}|$ is the magnitude. P is the period of the lattice and i is the diffraction order. Next, the magnitude of the transmitted beam and the momentum in the propagation direction, z, can be evaluated as,

$$k_t^2 = k_{i,z}^2 + (k_{i,x}\hat{x} + G)^2 \implies k_{i,z} = \sqrt{k_t^2 - (k_{i,x} + G)^2} \tag{3.3}$$

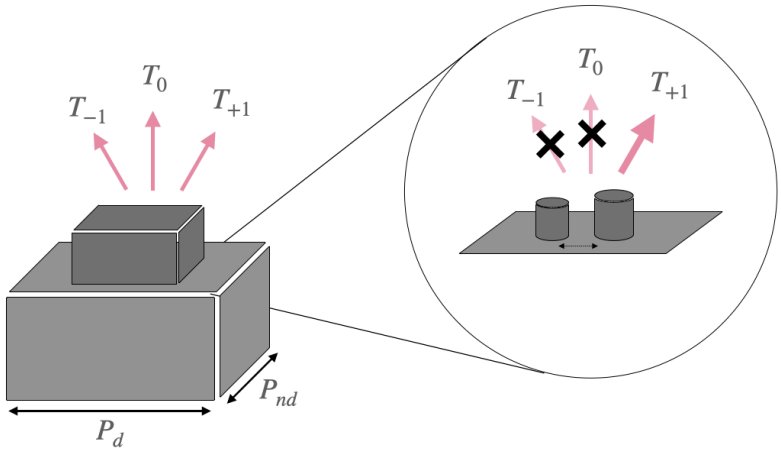

Figure 3.4: Supercell with a period that opens up the transmission orders T_0, T_{+1} and T_{-1} in one direction. The inset shows a sketch of how the meta-atom can be designed for desired energy distribution. The dashed arrow visualizes how the position of the pillars can be changed to get the wanted interference.

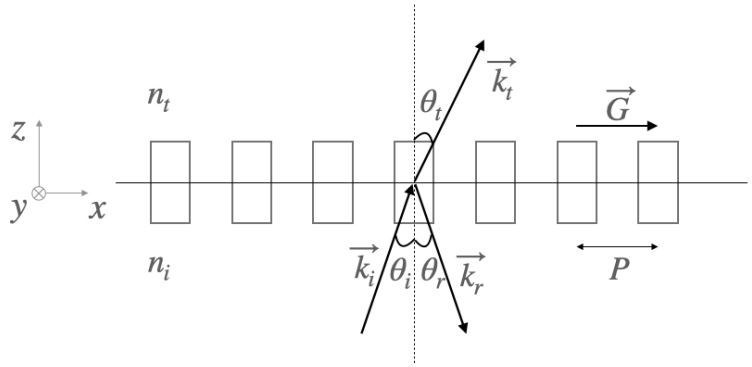

Figure 3.5: One dimensional diffractive grating at the interface of two media (refractive index n_i and n_t), with a period P and a reciprocal lattice vector $\vec{G}$. The incident, reflected and transmitted light is represented by their momentum $(\vec{k_i}, \vec{k_r}, \vec{k_t})$. The reciprocal lattice vector, $\vec{G}$, only adds momentum in the plane of the grating (x).

To transfer energy into a certain diffraction order and not have an evanescent field, $k_{i,z}$ can't be imaginary, which gives,

$$k_t^2 - (k_{i,x} + G)^2 > 0 \implies k_t^2 > (k_{i,x} + G)^2 \tag{3.4}$$

From Equation 2.2 together with $\lambda = \frac{\lambda_0}{n}$, where n is the refractive index, and assuming a plane wave with orthogonal incident ($k_{i,x} = 0$), the condition for which diffraction orders that are opened can be written as,

$$\left(\frac{n_t}{\lambda_0}\right)^2 > \left(\frac{i}{P}\right)^2 \implies P^2 > \left(\frac{\lambda_0}{n_t}\right)^2 i^2 \tag{3.5}$$

The same calculations apply to the reflected momentum, with the difference being the refractive index, since the transmitted and reflected wave propagates through different media. This means that different number of orders can be diffracted for transmission and reflection.

$$P^2 > \left(\frac{\lambda_0}{n_i}\right)^2 i^2 \tag{3.6}$$

Equations 3.5 and 3.6 states a condition for the size of the period to transfer energy into a certain diffraction order. However, when it comes to diffractive metasurfaces and diffractive elements, the grating equation also needs to be considered, since it sets the deflection angle.

$$n_t \sin\theta_t - n_i \sin\theta_i = \frac{i\lambda_0}{P} \qquad \text{or} \qquad k_t \sin\theta_t - k_i \sin\theta_i = \frac{i2\pi}{P} \tag{3.7}$$

From the transmission grating equation (Equation 3.7), the critical angle can be calculated. The critical angle is when $\theta_t = \frac{\pi}{2}$.

$$\theta_t = \frac{\pi}{2} \implies \sin\theta_i = \frac{1}{k_i}\left(k_t - \frac{i2\pi}{P}\right) \tag{3.8}$$

Above $\theta_t = \frac{\pi}{2}$, the diffraction order can only couple into an evanescent wave and does not transfer energy. This means that even if the period is large enough to create higher diffraction orders, the angle might be to large and hence that diffraction order does not transfer energy. This can be derived mathematically by looking at the condition for when the transmitted wave is propagating, again in one dimension, starting with the expression as in Equation 3.2.

$$\begin{aligned}
&\vec{k_t} = k_{t,z}\hat{z} + k_{t,x}\hat{x} \implies k_{t,z}\hat{z} = \vec{k_t} - k_{t,x}\hat{x} \\
\implies &k_{t,z} = \sqrt{k_t^2 - k_{t,x}^2} = \left\{k_{t,x} = k_t \sin\theta_t\right\} = \sqrt{k_t^2 - (k_t \sin\theta_t)^2} \\
= &\left\{\text{Equation 3.7}\right\} = \sqrt{k_t^2 - \left(\frac{i2\pi}{P} + k_i \sin\theta_i\right)^2} \\
\implies &k_t^2 > \left(\frac{i2\pi}{P} + k_i \sin\theta_i\right) \implies \sin\theta_i < \frac{1}{k_i}\left(k_t - \frac{i2\pi}{P}\right) = \frac{1}{k_i}(k_t - G)
\end{aligned} \tag{3.9}$$

The last implication is what is stated in Equation 3.8. Considering a plane wave propagating orthogonal to the grating, $\theta_i = 0$, the following expressions can be obtained

$$\begin{aligned} 0 < \frac{1}{k_i}\left(k_t - \frac{i2\pi}{P}\right) &= \frac{n_t}{n_i} - \frac{i\lambda_0}{n_i P} \\ \implies \frac{i\lambda_0}{n_i P} < \frac{n_t}{n_i} &\implies \frac{\lambda_0}{n_t} < \frac{P}{i} \end{aligned} \tag{3.10}$$

The last inequality determines possible diffraction orders where energy can be transferred.

A great advantage with metagratings is that it is, in theory, possible to get the transmission to be one [16]. The supercell metasurface approach has previous been used to create a lens with a numerical aperture close to unity [17]. In that work they used pillars made of Si on top of SiO_2 to cancel out unwanted diffraction orders. Depending on the angle and therefor the length of the period, different numbers of pillars were used. A similar work, but in one dimension, has also been shown to be successful [2]. In this case a grating made in GaAs was used to deflect with an angle of 60°, which in addition was integrated on a VCSEL. On the other hand, a problem with the supercell metasurface is that it can be hard to deflect small angles with good efficiency [15] [17]. For smaller angels the period becomes larger, and looking at Equation 3.5 or 3.6, more diffraction orders appears. This in turn means that there are more orders to cancel out which adds difficulties. To be able to build a lens with high numerical aperture, where angles from almost 90° to 0° needs to be covered, a mix of dynamic phase and supercell metasurface can be used [15] [17].

3.4 Meta-atoms

As mentioned previously, there are many ways in which a meta-atom can be created. Different shapes like pillars, fins, V-shapes, apertures and holes can be made [4] [13]. Further, the material can also be varied in many ways to achieve the desired output. In this project however, GaAs is the only material used. Previous work, using this material system only, have created shapes like GaAs nano-pillars with varying radius and gratings [2] [3]. However when creating the various shaped pillars the spacing between them will vary through out the surface. This gives rise to a fabrication issue when etching through the GaAs substrate which is called aspect ratio dependent etching (ARDE). It means that wider spacing will give deeper etching. To circumvent this problem an etch stop layer could be integrated in the GaAs substrate. However that is not desirable since one of the advantages with GaAs metasurfaces is that they can be monolithically integrated to the backside GaAs substrate of a VCSEL.

Another way around it is to create a design that avoids the problem of ARDE. This has been done in a previous work where gratings in GaAs have been designed and

fabricated with equal slit distances [2]. However, using a grating makes it only possible to deflect light in one dimension, not two which is desirable if a focus point is wanted. In this thesis, nano-holes with the constraint that they all should have the same radius, are used. The holes are etched into the GaAs substrate and thus consists air. The holes will be used as structures in the supercell approach, or diffraction based metasurface, for large angle deflection. The phase delay, diffraction and interference effects will be set by the distances between the holes, the radius and depth of the holes. Nano-holes have previous been used to support different resonances in dielectric materials and for biosensing using silicon [18] [19]. As mentioned in the previous section, a mix of supercells and dynamic phase metasurfaces could be needed for a metalens covering all angels. For the dynamic phase metasurface, the phase delay is controlled by the size of the meta-atom, hence the issue of ARDE could reappear using holes. A way around this could be to make the height of the hole a function of the radius, $h_{meta}(r)$, based on experimental etching rate, and then map the phase delay to that function.

4

Design and simulations of metasurfaces

This section starts with a description of the finite element method (FEM) and the used software COMSOL Multiphysics. Next, the set-up of the structure and verification of the simulation model is described. Finally, the optimization of the geometry to get the desired light deflection is presented together with the results of the optimization.

4.1 The finite element method

The finite element method (FEM) is a numerical simulation method normally used for solving differential equations [20]. It is commonly used in electromagnetics to solve Maxwell's equations. To compute the electric field in a domain, FEM discretizes the geometry into small finite elements, or subdomains, which are smaller and simpler in shape. The field is then calculated in each domain and expressed as low-order polynomials. Hence, the field of the whole domain is represented by piecewise functions. That way of describing the field is not normally enough to, together with the boundary conditions, fulfill e.g. Maxwell's equations pointwise. What FEM does, instead of finding a pointwise solution, is to find an averaged solution for the electric field to satisfy the differential equation and the boundary conditions. A great advantage with FEM is that it can deal with complex geometries when dividing it into subdomains, creating unstructured grids called meshes. A problem with FEM is that it requires a lot of computational memory.

4.2 Simulation in COMSOL

In this work the software COMSOL Multiphysics, which utilizes FEM, has been used to solve Maxwell's equations for the metasurfaces. One period, or cell, of the whole metasurface has been modeled in COMSOL by setting up the material properties and geometry of the meta-atoms. One period consist of between three and four nano-holes and then periodic boundary conditions, assuming an infinite lattice of the same supercell, have been used in the transverse direction. In the longitudinal directions ports were set up which at the bottom excites the cell with an electromagnetic wave and measures the propagated wave at the top.

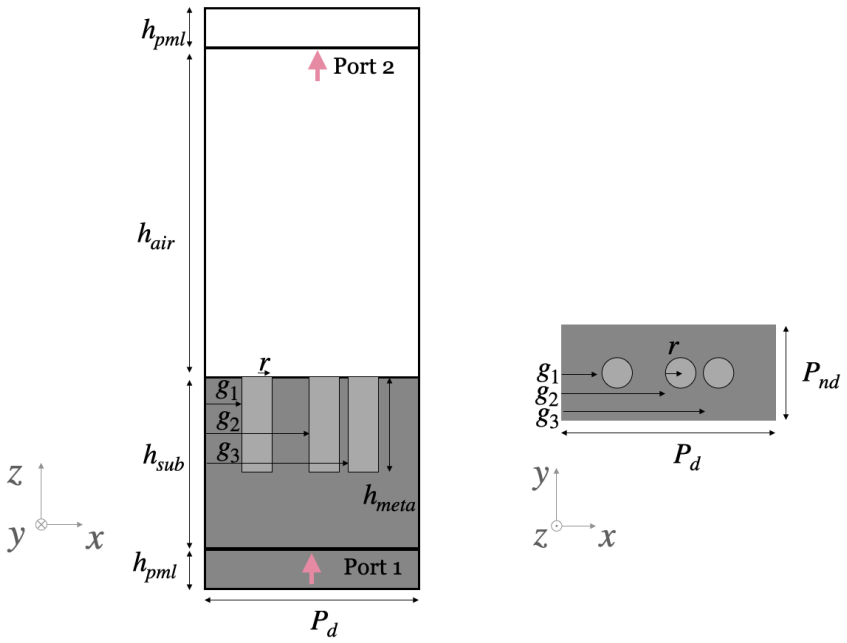

Figure 4.1: Sketch of a supercell that was simulated in COMSOL and used for the diffraction based metasurface. The left figure shows the cell from the front and the right figure is from the top.

The supercell structure used in the simulations were made of building blocks in different materials and can be seen in Figure 4.1, where all dimensions are marked. Staring from the bottom, there are two blocks of GaAs which represents the substrate. The first block is a perfectly matched layer (PML) and will be discussed later in this section. Put into the substrate are pillars filled with air, making up the nano-holes. On top of everything are two blocks of air, again the top one is a PML. The ports are located at the out-pointing interfaces of the inner substrate and air blocks, see 'Port 1' and 'Port 2' in Figure 4.1. Since the supercell is designed to be diffractive the ports were set up to be able to measure several diffraction orders.

4.2.1 Meshing, boundary- and start conditions

Since FEM divides the structure into smaller elements, also known as meshing, the following condition was used to decide the maximum allowed element size,

$$l_{max} = \frac{\lambda_0}{n c_{mesh}},$$

where λ_0 is the wavelength of the exiting wave, n is the refractive index of the domain and c_{mesh} is a positive integer that determines the discretization of the wavelength, where a larger value gives a result closer to the continuous value. Before any optimization of the geometry of a supercell was done, convergence studies of the mesh was made to find out a sufficient value of c_{mesh}. The convergence study of c_{mesh} can be found in appendix A.1.1.

Since only one cell of a whole metasurface is simulated, a periodic boundary condition in the transverse direction is assumed. The periodic boundary condition was fulfilled by making sure that the meshing at opposite sides (transverse direction) of the structure were the same. For the excitation of the cell, starting conditions were set up. To ensure that the ports in the model were properly set up convergence studies of the height of the substrate (h_{sub}) and height of air above the substrate (h_{air}), see Figure 4.1, were made. The ports are set up to be continuous (Robin boundary condition) and by doing this study one makes sure that all evanescent waves are absorbed. The convergence study of h_{sub} and h_{air} can be found in appendix A.1.2.

4.2.2 Perfectly matched layers

A perfectly matched layer (PML) is an artificial domain that can be added in simulations to truncate regions, often with open boundaries, where computations are made. The domain has a refractive index that is made to attenuate all propagating waves, which can be used to simulate the appearance of a structure surrounded by free space. As can be seen in Figure 4.1, there are two blocks of PML, one made of air and one of GaAs, both with the height h_{pml}. The PML were added to faster reach the free space condition to be able to measure all diffraction orders properly and to be able to put the ports closer and in turn get a faster simulation. To decide the thickness (h_{pml}) of the PML, which properly absorbs the electromagnetic wave, a study of the electromagnetic field for different thicknesses was made. The result can be found in appendix A.1.3.

4.3 Optimization of Supercell

Once the structure was properly set up, see Figure 4.1, optimization of the geometry, within the supercell, to get the desired constructive and destructive interference was carried out. The deflection angle is set by the period of the supercell. Note that the period in one direction, P_d is chosen to be diffractive while the period in the other direction, P_{nd}, is picked to be non-diffractive. As a starting point, geometries from previous similar works were considered [2] [3]. Following this, the optimization module in COMSOL together with parametric sweeps were used. The distances (g_1, g_2 and g_3) between the holes, the radius (r) and height (h_{meta}) of the holes, see Figure 4.1, were optimized. The used optimization algorithm was the Nelder-Mead method, which is a direct search method based on function comparison. In all simulations, the structure was first excited with and optimized for linearly in-plane polarized light and then optimized for both in-plane and out-of-plane polarized light.

In Figure 4.2 the simulated E-field, of a supercell with an optimized geometry for in-plane polarized light, can be seen for the deflection angle 61°. The relative transmission, η, for the first transmission order (T_{+1}) was 96% and the total transmission (T_{tot}) was 61%. The optimized dimensions can be seen in Table 4.1. Optimization of angles between 85° and 31°, with steps of 1° were carried out and the results can be seen in appendix A.2. 31° was picked as the lower limit since the periodicity for angles below that, makes the second diffraction order appear. The upper limit, 85°,

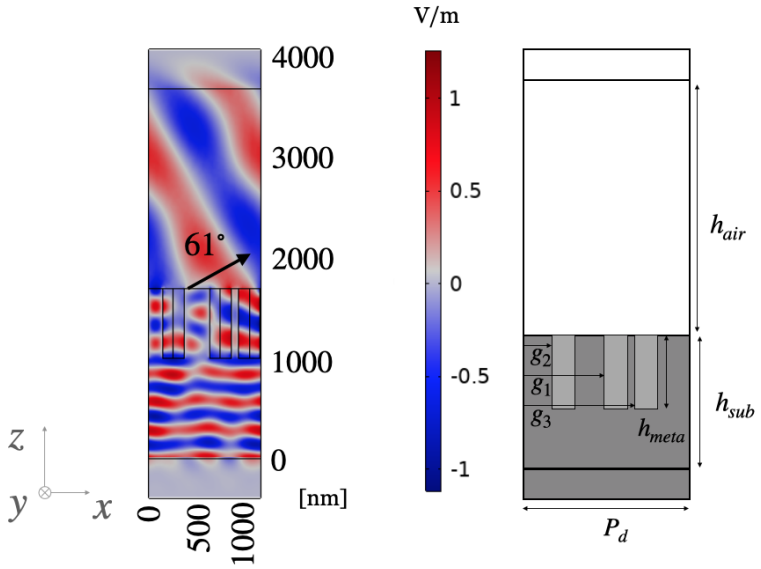

Figure 4.2: The simulated E-field in a supercell that deflects light with 61°. In the E-field the created interference pattern can be seen. The E-field plot is normalized and shows the in-plane (x) polarization.

was considered to be large enough and since the diffracting period (P_d) only changed with 1 nm or less for larger angles, it could be difficult to fabricate it. The choice of angle discretization was based on previous work [15] [17]. Initially the radius and height of meta-holes were included in the optimization for a range of angels. When the radius and height were considered to be good and joint for those angles, they were kept constant ($r = 110$ nm and $h_{meta} = 700$ nm) for the rest of the optimization and only the distances (g_1, g_2 and g_3) between the holes were included. The reason for that was to fulfill the constraint of a constant radius to circumvent ARDE and it also made the optimization algorithm more efficient and faster. Since the structure varies between the different cells with different angles, the relative transmission and total transmission also fluctuates. Even though the goal of course was to get it as high and equal as possible.

Table 4.1: Optimized dimensions for 61°, considering only in-plane linearly polarized light. The definitions of the parameters can be seen in Figure 4.1.

Dimension	Length
g_1	136 nm
g_2	609 nm
g_3	904 nm
h_{meta}	700 nm
r	110 nm
P_d	1125 nm
P_{nd}	240 nm

Since the VCSEL emits linearly polarized light in one plane, one has to consider two planes when creating a spherical lens due to the fact that the supercell has to be rotated in that design. This will be described more in detail in the Characterization chapter. Therefor a second optimization, considering both in-plane and out-of-plane polarized light was carried out, also in the range between 85° and 31° with integer steps. The optimization was done using the dimensions from the previous optimization with only in-plane polarization, as starting values. Again, the radius and height of the holes were set to be, $r = 110$ nm and $h_{meta} = 700$ nm. For the deflection angle 61° the in-plane relative transmission, η, for the first transmission order (T_{+1}) was 90 % and the total transmission (T_{tot}) was 68 %. The out-of-plane relative transmission, η, for the first transmission order (T_{+1}) was 78 % and the total transmission (T_{tot}) was 34%. The dimensions of that deflection angle can be seen in Table 4.2. Comparing with the optimization for only in-plane polarized light, the total transmission is lower. Furthermore, it is harder to get equally high total transmission for in-plane and out-of-plane transmission using this geometry, even though the relative transmission is similar. The results of the optimized dimensions for the rest of the angles can be seen in appendix A.2.

Table 4.2: Optimized dimensions for 61°, considering both in-plane and out-of-plane linearly polarized light. The definitions of the parameters can be seen in Figure 4.1.

Dimension	Length
g_1	103 nm
g_2	592 nm
g_3	884 nm
h_{meta}	700 nm
r	110 nm
P_d	1125 nm
P_{nd}	240 nm

Based on the simulations of the supercell, patterns were created that was later used in the fabrication process. Different patterns for metasurfaces with different functionalities were made and will be described in the Characterization section.

5
Fabrication of GaAs metasurfaces

This chapter starts with an overview of the fabrication route of GaAs metasurfaces, and the machines and techniques used in each step. Following that, the results from an optimization process that was carried out for the dry etching (Inductively Coupled Plasma-Reactive Ion Etching) will be presented.

5.1 Process route

In this section the clean room fabrication route for the metasurfaces will be described and theory of each process step will be explained. The goal of the fabrication is to create nano-sized structures in a GaAs-chip. The process follows a positive electron-beam lithography route that can be seen in Figure 5.1. Note that the fabrication of metasurfaces is first done on a plain GaAs chip, without any VCSEL, to optimize and try out different metasurfaces, and then integrated on the backside of a VCSEL when the desired metasurface has been fabricated. The fabrication starts with cleaning of the GaAs chip, followed by a reactive sputtering of SiO_2. After that, resist is spinned, exposed and developed, on top of the SiO_2 layer. Subsequent the development, a lift-off is made to create a metal mask of Cr and Ni. Dry etching is then used to etch through SiO_2 and GaAs. Finally, etching with HF is made to remove SiO_2 together with the evaporated metal.

5.1.1 Standard solvent cleaning

The chips used in this fabrication process were diced from a GaAs wafer with a thickness of 0.5 mm. Once the desired chip size was acquired, typically 1×1 cm^2, solvent cleaning of the chip was done to make sure that no dirt or small GaAs particles would remain on the surface. The used standard solvent cleaning process consists of three steps. First, the chip is put in a beaker with acetone at 50 °C during 5 minutes. Then the chip is taken out and sprayed with acetone, using a spray gun. Secondly, the chip is put into a beaker of methanol for 5 minutes. Finally, the chip lays in a beaker of isopropyl alcohol (IPA) for 3 minutes and is then blow dried with nitrogen gas (N_2).

5.1.2 Sputtering

Once the chip was cleaned, reactive sputtering of SiO_2 was made. This was done using a sputter machine in the clean room at Chalmers. Sputtering is a physical

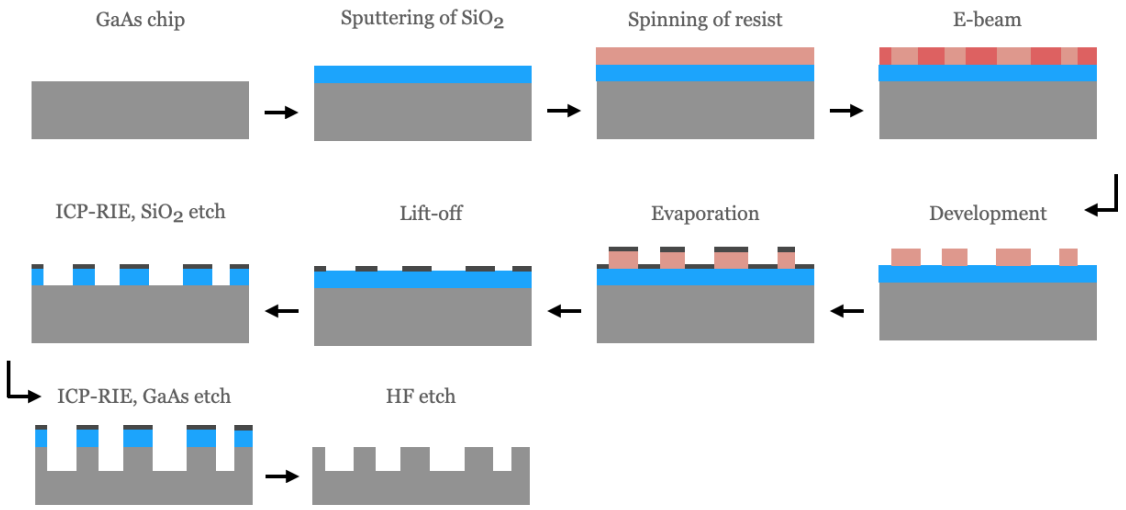

Figure 5.1: Process route used for fabrication of metasurfaces. The route starts with reactive sputtering of SiO_2. Then Electron Beam Lithography (EBL) is used to create a mask, including spinning of resist, pattern writing with an electron-beam machine and development of the resist. Following that, metal evaporation and a lift-off is made to create a metal mask to get higher selectivity. Finally, dry etching through SiO_2 and GaAs followed by etching with HF to remove remaining SiO_2 and metal, is done.

vapor deposition (PVD) method to, for instance, deposit thin film layers. Surface atoms, from a sputtering target material, are ejected by bombarding the surface with energetic particles that can be a gaseous ions that are accelerated from a plasma. The ejected atoms are then deposited on the substrate or chip.

DC or RF sputtering are the two most common sputtering methods, which differ by the power source, using a direct or alternating current. Using RF sputtering prevents charge build up and was used in this fabrication. The target material and substrate to be deposited, are placed in parallel inside a vacuum chamber [21]. An inert gas, often Ar, is injected into the chamber. An RF current is applied between the target material (cathode) and the substrate (anode). The Ar atoms are first ionized, which makes the positive ions collide with the negative target material ejecting atoms into the plasma. The electrons in the plasma are then, together with the ejected atoms of the target material, attracted to the positively charged substrate, where they will condense and create a thin film on the substrate, see Figure 5.2.

Using conventional sputtering, single element materials can be deposited efficiently. However, if a compound like SiO_2 is wanted, reactive sputtering can be used. In addition to the inert gas, a non-inert gas, like O_2 in this case, can be used [22]. The non-inert gas chemically reacts with the ejected atoms of the target material, Si in this case, and creates a compound material which is then deposited on the substrate. To get the desired thickness of the sputtered film, parameters like time and power can be changed. In this project 112 s and 1 kW were used to achieve a SiO_2

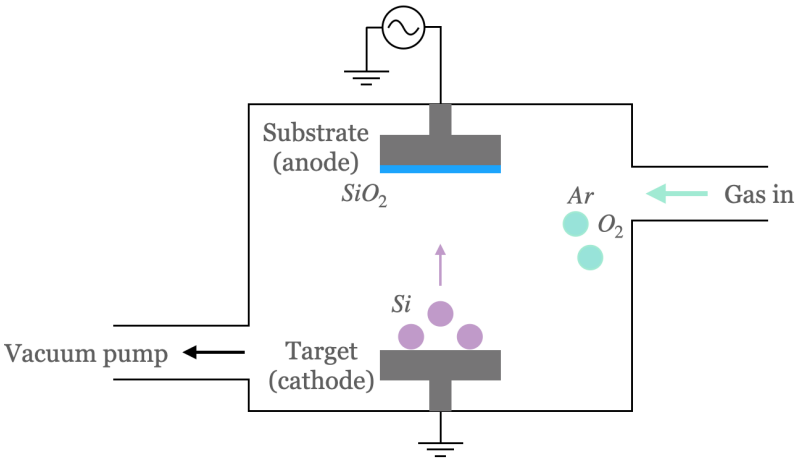

Figure 5.2: Sketch of a sputtering machine. The injected Ar atoms are ionized by the applied electric field between the cathode and anode. Surface atoms from the Si target are then ejected under bombardment of accelerated Ar ions. The Si atoms react with the injected O_2, creating SiO_2 which then forms a film (blue) on the substrate.

thickness of 25 nm. To make sure that the thickness was correct, a measurement in an ellipsometer was made.

5.1.3 Electron-abeam lithography

Subsequent the sputtering of the SiO_2-layer, electron-beam lithography (EBL) was used to create a mask of the pattern designed for the metasurface. In EBL, a focused beam of electrons is scanned over a surface with a film that is sensitive to exposure of electrons. With EBL, patterns with small features, < 50 nm, can be created and then transferred into a material, using for instance etching.

The first step in the lithography process is to spin resist on the chip. Prior to the spinning the chip was heated to evaporate any residuals from the cleaning. This was followed by a deposition of hexamethyldisilazane (HDMS), to improve the adhesion of the resist. The used positive resist was ARP6200 (1:1) and the spinning lasted 45 seconds using a speed of 4000 rpm and an acceleration of 1000 rpm/s, which created a 125 nm thick resist layer. After spinning, a soft bake was done at 160° for 5 minutes. The purpose of soft baking is to evaporate the solvent from the resist and enhance the adhesion of the resist on the chip.

Next in EBL, an electron-beam writes the pattern by exposing the resist. The molecules in the exposed areas are degraded, while the unexposed stay in their original state. In the following step, when the resist mask is developed, the exposed (degraded) parts are dissolved by the developer. The used developer was n-Amyl acetate. When writing the pattern, there are several parameters that can be changed. One of them is the electron dose of the beam. It is important that the dose is high enough to get sufficient exposure. Therefore a clearence test was made, where the

depth of the developed parts of a test pattern, exposed with different doses, was measured with a profilometer. The test can be seen in appendix B.1 and shows that a dose of at least 180-200 $\mu C/cm^2$ is needed. More over, the step size, beam current and beam aperture were investigated during the metasurface fabrication to find out which parameters gave the best optical performance during the characterization.

5.1.4 Metal mask

To get a higher etch selectivity of the mask versus GaAs for the following etching a metal mask was created, replacing the resist mask. This was done by first evaporating 100 Å Cr followed by 500 Å Ni. Then a lift-off was made, by submerging the chip into the remover MR-Rem 400. The remover dissolves the remaining unexposed parts of the resist, lifting off the metal that is on top of it. The metal that was evaporated directly on the SiO_2-layer is left, having the same pattern as the exposed resist. Ni is used since it has a high etch selectivity compared to GaAs. A layer of Cr was added underneath to get better adhesion of Ni, to make the lift-off process easier.

Evaporation is a physical vapor deposition (PVD) method. For the evaporation that was used in this project, an e-beam thin film evaporator was used. In the evaporator an electron beam is created, often by charging a tungsten filament. The beam is then directed to a crucible with the wanted material, using a magnetic field. The beam heats the content of the crucible, making it evaporate. The chip is placed on a holder above the crucible inside a vacuum chamber, see Figure 5.3. When the evaporated material reaches the sample holder with the chip, it forms a thin solid film on it. Compared to the sputter machine, the e-beam makes it possible to reach very high temperatures which is why metals with high melting points can be used. Further, evaporation is a very directional deposition technique, in comparison to sputtering, which gives poor sidewall coverage, which in turn is suitable for a lift-off process.

5.1.5 Inductively Coupled Plasma-Reactive Ion Etching

To transfer the pattern into the GaAs-substrate, dry etching, or more specific Inductively Coupled Plasma-Reactive Ion Etching (ICP-RIE), was used. The etching was done in two steps, first to etch through the SiO_2-layer and then through GaAs.

For the etching of SiO_2, Fluorocarbon gas (CF_4) is injected to a vacuum chamber where the chip also is placed. In the chamber, Flourine atoms become ionized and reacts with Si, creating gases like SiF_4. To make the etch rate faster, O_2 is also injected. This creates gasous compounds like CO, CO_2 and COF_2. The created gases are vented out from the chamber and SiO_2 is etched wherever there is no metal mask. The chemical reactions are summarized in Figure 5.4. To know how long the etching of SiO_2 should be to get through the used layer of 25 nm a laser interferometer was used to measure the thickness while the etching was ongoing.

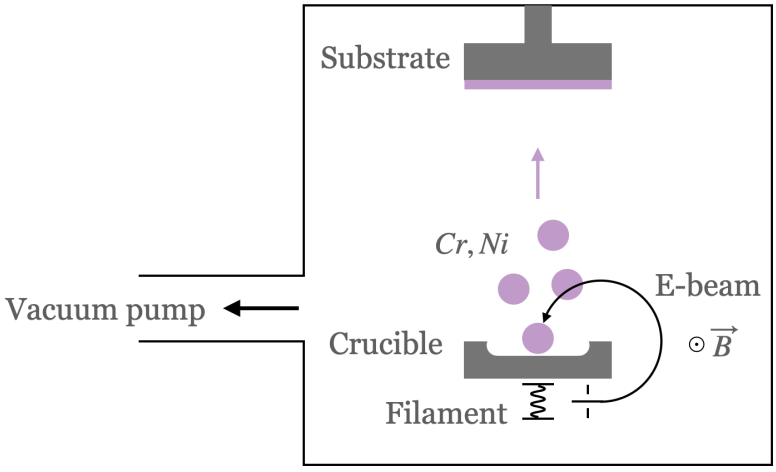

Figure 5.3: Sketch of e-beam thin film evaporator. An electron beam is created by charging a tungsten filament. To target the crucible, with the metal to be evaporated, the beam is bent by a magnetic field ($\vec{B}$). The electron beam evaporates the metal, Ni and Cr, which forms a film on the substrate.

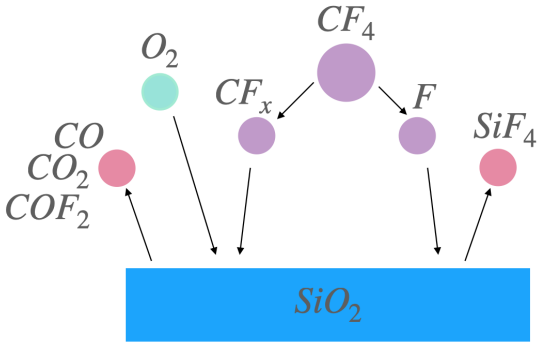

Figure 5.4: Summary of the chemical reactions for ICP-RIE of SiO_2. CF_4 is injected to a vacuum chamber and creates compounds like F and CF_X. The flour atoms reacts with Si in the SiO_2 layer (blue) creating gases such as SiF_4. O_2 can also be injected into the chamber to increase the etch rate, by creating gaseous compounds as CO, CO_2 and COF_2.

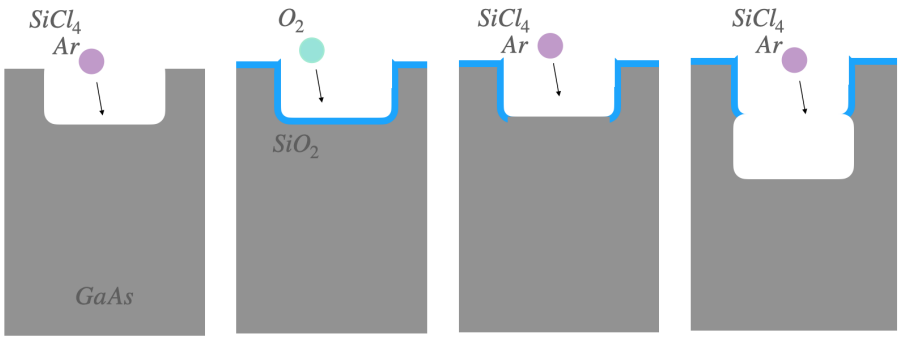

Figure 5.5: Etching of GaAs, mimicing the Bosch process for Si. The figure shows the three steps that are included in each cycle of the etching. First, to the outermost left in the figure, GaAs is etched through physical and chemical reactions with $SiCl_4$ and Ar. Secondly, O_2 is injected, forming a passivation layer of SiO_2 (blue), seen in the second block from left in the figure. In the third step, third block in the figure, the bottom of the passivation layer is etched away by $SiCl_4$ and Ar, and kept at the side walls. The forth block shows the first step in the following cycle where GaAs is etched with the walls protected. This type of etching is used to etch narrow and deep trenches.

Once the layer of SiO_2 was etched away, etching of GaAs followed. This etching is a deep reactive-ion etching, using a processes that mimics the Bosch process for Si, which makes it possible to etch deep with vertical walls. The Bosch process contains three steps that are cycled, see Figure 5.5. The first step is GaAs etching, using $SiCl_4$ and Ar. $SiCl_4$ forms Si and Cl_2. Cl_2 then chemically etches GaAs, while Ar ions are accelerated to physically knock out atoms in GaAs. Next, a descum step is made via injection of Ar to remove residue compounds. In the second step, a passivation layer of SiO_2 is formed on the side walls and the bottom of the trench, by injecting O_2 that reacts with the remaining Si from the first step. Thirdly in a final step, the passivation layer at the bottom is etched away by injecting $SiCl_4$ and Ar. The reason to why only the bottom part of the passivation layer is etched, is presumably because of anisotropic etching of SiO_2, favoring vertical over horizontal etching. This is probably achieved by either the Ar ions being accelerated vertically and therefor also etch in that direction or $SiCl_4$ doing anisotropic etching of SiO_2. The steps are then cycled, so in the first step of the following cycle, the walls are protected while the bottom gets etched which makes it possible to create deep and narrow trenches.

A problem with the Bosch etching is that as the etching gets deeper, the side walls tends to become tilted inwards, making the hole V-shaped. The reason for this is that the access angle to the bottom becomes steeper as the etching gets deeper. To get rid of this, or to minimize the tilting, the etching recipe was optimized. There are many parameters that can be adjusted in Bosch etching, like time, power, amount of gas injected to the chamber and chamber pressure. The optimization that was made focused on the etching time. By using a longer etching time during the last cycles of the etching, the walls seemed to get more straight. As a starting point a

previous recipe was used. In Figure 5.6, scanning electron microscope (SEM) images of etched gratings using the original and the optimized receipt can be seen.

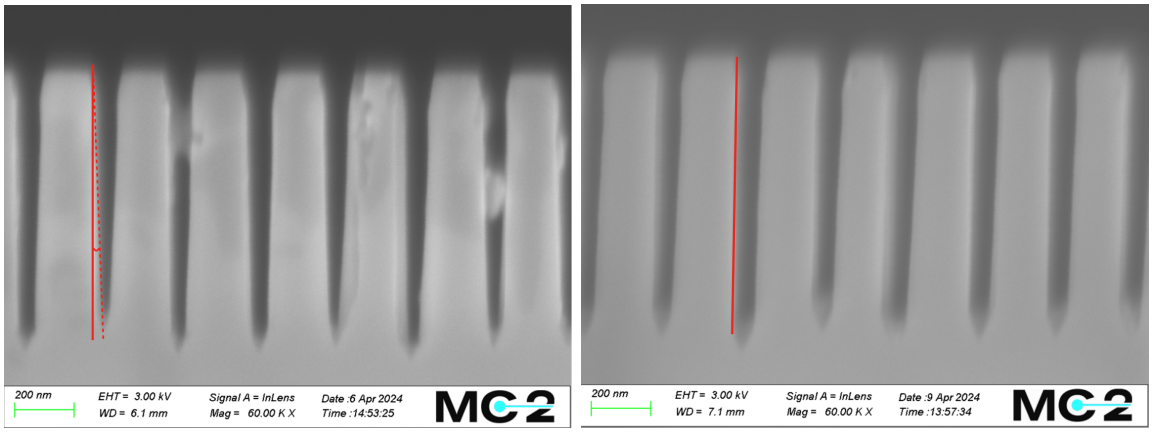

(a) **(b)**

Figure 5.6: SEM pictures of (a) original and (b) optimized recipe of ICP-RIE of GaAs. As is visualized with the red lines, the walls in (b) are kept more straight as the trench gets deeper in comparison to (a) where the trench becomes narrower with depth. The optimized recipe uses longer etching times in the last cycles.

5.1.6 Wet etching with HF

As a final step, wet etching with Hydrofluoric acid (HF) was done. HF dissolves SiO_2 and the remaining exposed parts of the resist, which also removes the metal mask on top of it. This leaves a chip with only GaAs with the designed pattern etched into it. The chip was submerged into HF, diluted to 2 %, for 1 minute.

5.2 Fabricated metasurfaces

Different types of metasurfaces, containing only one type of supercells and surfaces with supercells for various deflection angles making up lenses, were fabricated, according to the design from the COMSOL simulations. The types of metasurfaces will be described further in the Characterization chapter. In Figure 5.7 SEM pictures of the hole pattern of the supercells of a metasurface can be seen. As can be seen in the figure, the height of the holes are equal, meaning that the issue of ARDE was circumvented. The measured values for the periodicity of the supercell agree with the design. However, the size of the holes did not match the designed pattern, the fabricated radius (r) was smaller, 93 nm compared designed radius of 110 nm. Further, it was hard to control the etch depth of the holes (h_{meta}) in a precise manner. To understand how much the deviations in radius and height of the holes affected the transmission, COMSOL simulations were performed. The results for 61° can be seen in Figure 5.8 and show that some variation in size around the optimized values affects the transmission, especially the radius where a deviation

of e.g. 10 nm reduces the relative transmission (η) with 20%. Hence it was desirable to make the fabrication process more exact. To increase the radius of the fabricated holes, the radius in the pattern design was made larger, which made the radius of the fabricated holes closer to the wanted value, a radius of 102 nm was achieved. However there was still some deviation from the target radius of 110 nm, so it would be beneficial to polish the process route further or try some other path, like for instance to use a negative resist. Another issue with fabrication of the holes was that the edges of them sometimes got a bit rough. Trials to improve this by changing the write paths were carried out which helped to some extent. The use of a negative resist might help here as well, since that means that the e-beam machine writes circles rather than holes, which the e-beam software is better at fracturing for the writing path.

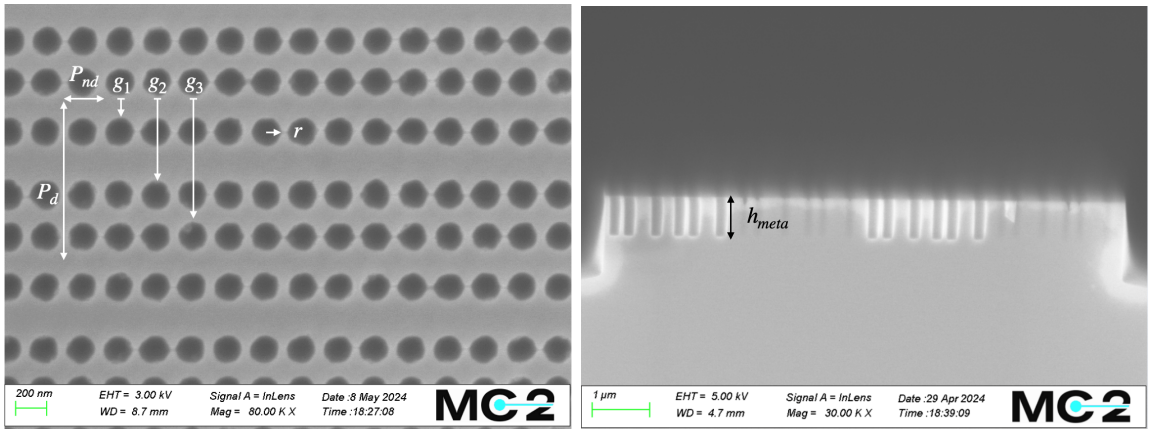

(a) **(b)**

Figure 5.7: SEM pictures of the fabricated hole structure, in (a) top view and (b) cross-section. The SEM pictures are taken of a metasurface containing supercells that should yield a deflection angle of 75°. The parameters P_d, P_{nd}, g_1, g_2, g_3, r and h_{meta} are marked.

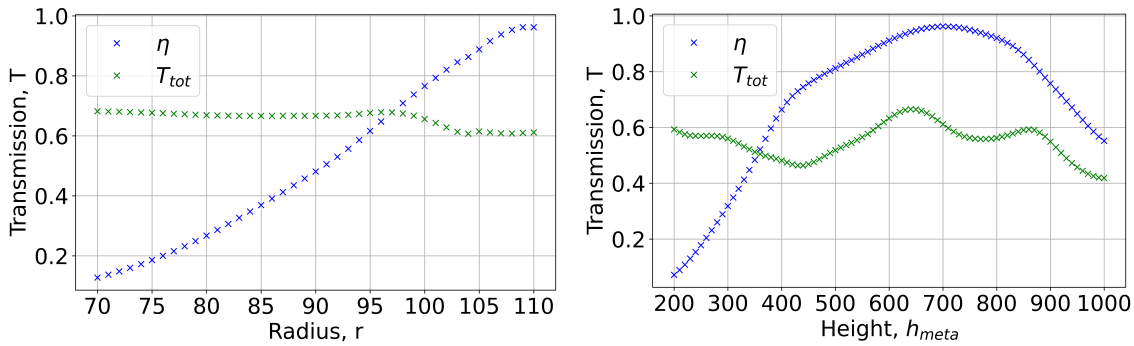

(a) **(b)**

Figure 5.8: Effect of meta-hole size on relative (η) and total transmission (T_{tot}); (a) shows a change in radius and (b) a change in height, of the meta-holes for a supercell yielding a deflection angle of 61°.

6

Characterization and comparison to simulations

In this chapter, results from characterization of the fabricated metasurfaces, together with simulations of light propagating through them, will be presented. Before that, a description of the set-up for the measurements will be given and an explanation on how the Fourier plane can be simulated.

6.1 Measurement set-up

A sketch of the measurement set-up that was used for characterization of the metasurfaces, can be seen in Figure 6.1. The set-up consist of a laser with linearly polarized light with the wavelength $\lambda = 976$ nm and an output power of 0.25 mW. The laser light is reflected twice by two mirrors, which does not affect the polarization, but changes the direction of the beam. Next, the beam passes through a lens with focal length $f = 10$ cm and a quarter wave plate. This is to create a quasi-collimated and narrow beam that is circularly polarized. Additionally, there is a linear polarizer which is used to make the polarization linear and select polarization direction (in-pane or out-of-plane). Following that, the approximately planar and linearly polarized beam, passes through the metasurface and is then gathered by an objective with NA=0.95. Before the light is captured by a camera, it is deflected by a mirror, passes through two lenses to get Fourier plane imaging, to see the spatial frequencies of the beam, this can be seen more clearly in the inset of Figure 6.1. The first lens, placed in the back focal plane of the objective, creates a Fourier transformation of the image in the objectives' focal plane, where the metasurface is placed. The same lens also focuses the parallel rays, from the objective, to the lens' focal point. The second lens is then used to focus the rays into the camera. Finally, two neutral density (ND) filters (NE60A-B OD 6.0 and NE15A-B OD: 1.5) are used to lower the intensity of the beam to avoid saturation when capturing. Exposure time of 10 ms was used in the camera. Since the numerical aperture of the objective was limited to 0.95, only metasurfaces with deflection angles smaller than 72° could be measured.

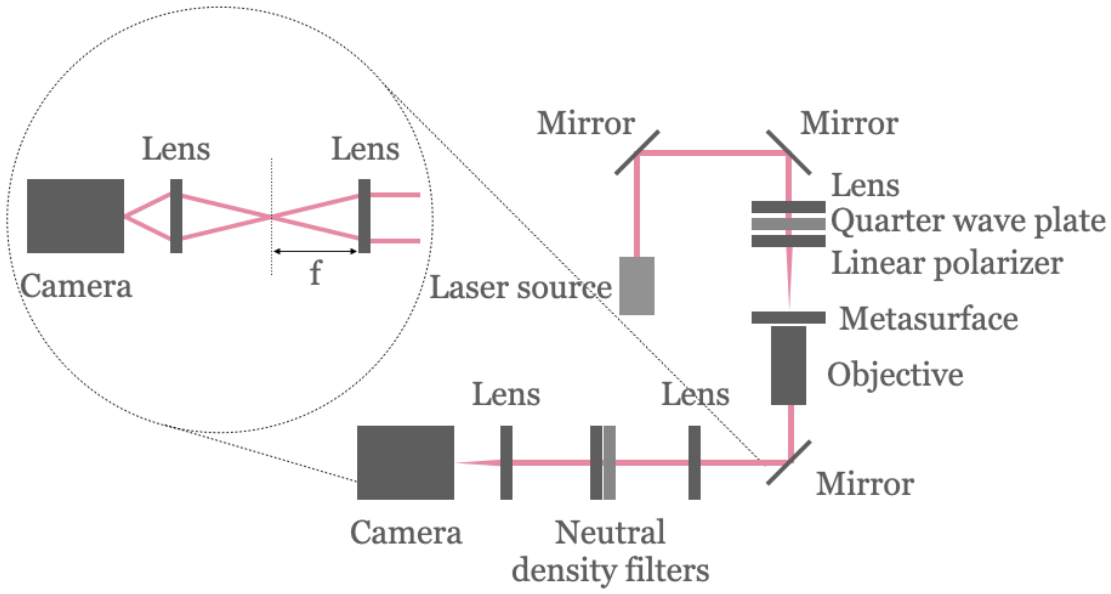

Figure 6.1: Sketch of the measurement set-up used for characterization of the metasurfaces. The set-up uses Fourier plane imaging, which is visualized by the inset.

6.2 Simulation of the angular distribution of the far-field (Fourier plane)

To simulate the angular distribution of the far-field, the so called Fourier plane, numerical methods can be used. One way is to sample the field of plane wave components in a starting plane, and then take the two dimensional Fourier transform, which will give the angular spectrum. Next, each plane wave is propagated to an end plane by multiplying with a propagation term, which adds the phase change of the propagation. In this case, the starting plane will be just after the metasurface and the end plane at the focal length of the metasurface if it is a lens. The metasurface is simulated by setting up its corresponding phase profile.

6.3 One type supercell metasurface

As an initial step in the fabrication of the optimized supercells, metasurfaces containing only one type of supercell, one deflection angle, with the same orientation were made, see Figure 6.2 for a sketch and Figure 6.3 for SEM images. This was done for several angles, using the optimized dimensions for in-plane polarization. In Figure 6.4, simulations together with the measured Fourier plane for the deflection angle 61° can be seen. The measurement shows that the intended deflection angle is achieved, however the destructive interference for the transmission orders T_{-1} and T_0 is not as good as in simulations, the measured relative transmission of those orders are 6.2% and 4.5%, respectively. In Figure 6.5 an integrated cross section from measurements of some angles between 35° and 70° can be seen, and in

Table 6.1 the simulated and measured relative transmission, for the same angles are given. There is still energy in the unwanted diffraction orders T_{-1} and T_0, which in addition results in a lower relative transmission compared to simulations. The difference between the real measured and the simulated values is most probably due to fabrication limitations. As can be seen in Figure 5.8, the deviation in parameter values affects the transmission and as discussed in the Fabrication chapter the radius of the fabricated holes tended to be smaller than the designed radius and also have some roughness at the edges, which can be seen in Figure 6.3.

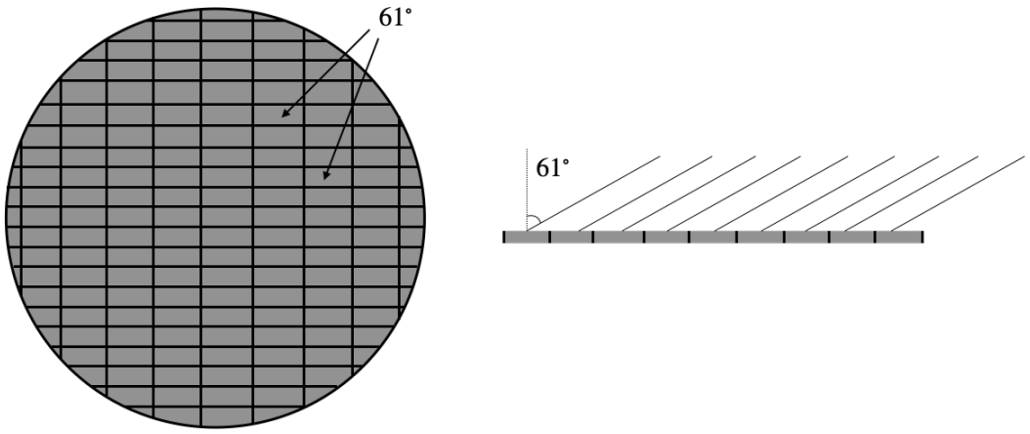

Figure 6.2: Sketch of a metasurface containing only one type of supercells, corresponding to one deflection angle. The supercells are placed in a grid, all oriented the same way. To the left is a sketch form above and to the right from the side.

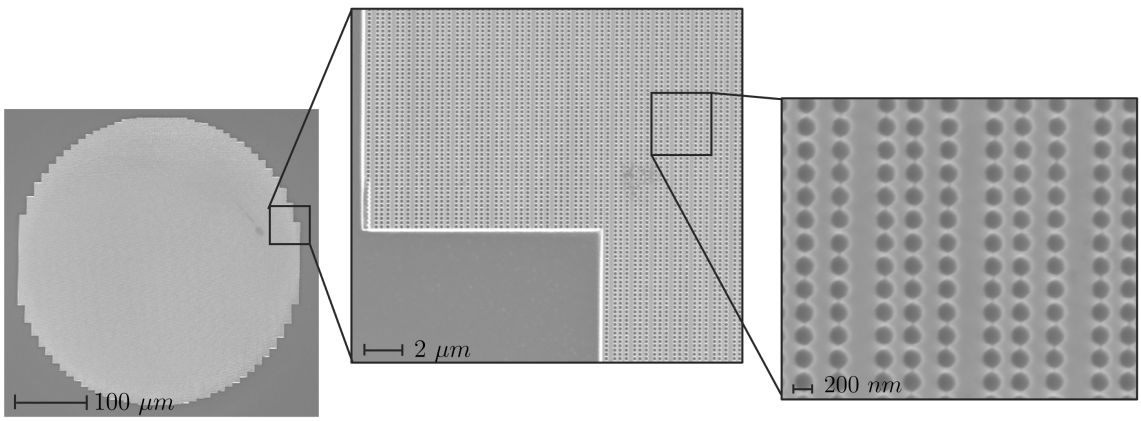

Figure 6.3: SEM images of a metasurface containing one type of supercell. The same type of supercell is used and placed with the same orientation.

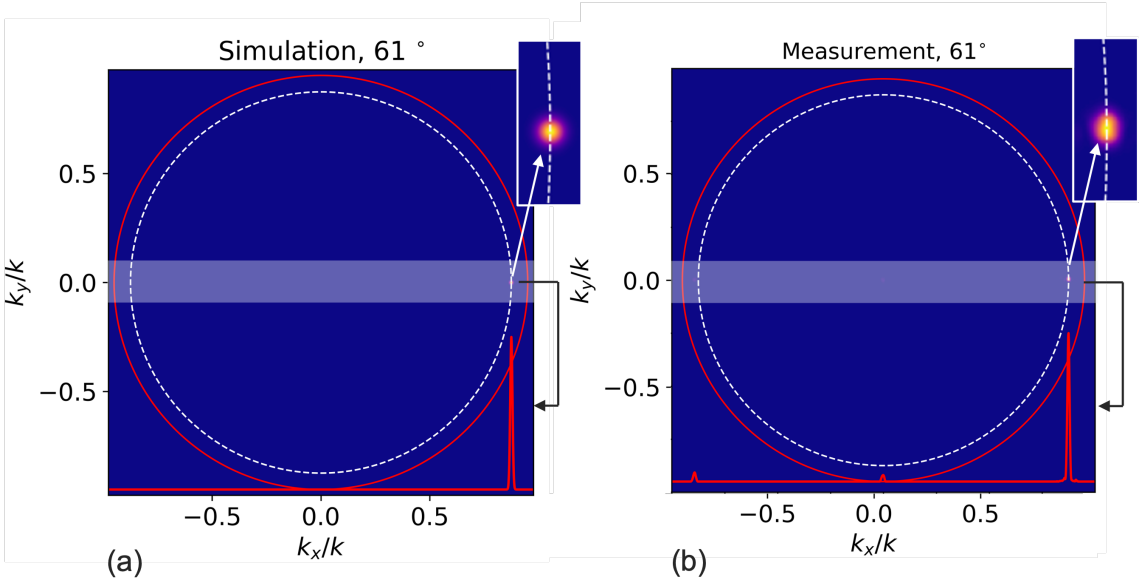

Figure 6.4: (a) Simulated and (b) measured Fourier images of a metasurface using only one type of supercells for deflection of 61°. The dashed white line marks the target angle, the red line the maximum collection angle. The red graph at the bottom shows the integrated intensity of the highlighted cross section, were the peaks from left to right corresponds to T_{-1}, T_0 and T_{+1}. The inset shows an in-zoomed image of the T_{+1} spot in the Fourier plane.

Table 6.1: Simulated and measured relative transmission (η) for T_{+1} for different deflection angles between 35° to 70°.

Angle	η (simulated)	η (measured)
35°	71.7%	67.8%
40°	91.0%	69.8%
45°	87.4%	79.8%
50°	90.4%	81.1%
55°	90.8%	68.5%
61°	96.0%	89.3%
65°	92.7%	94.7%
70°	91.2%	88.7%

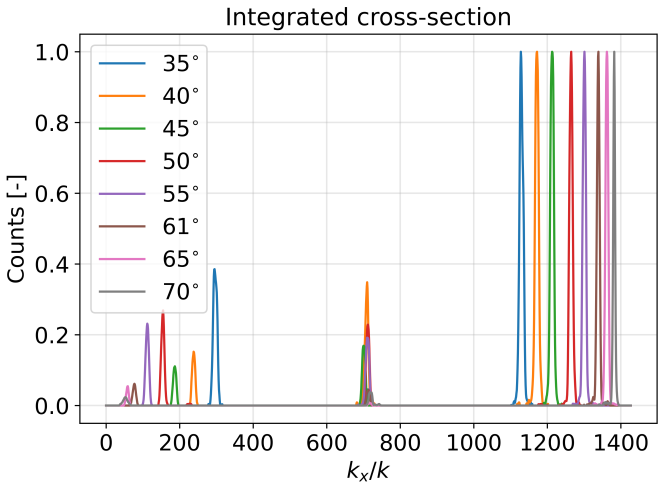

Figure 6.5: Integrated cross-section of the measured Fourier plane for the angles 35° to 70°. The peak to the left corresponds to transmission order T_{-1}, the middle one to T_0 and the one to the right to T_{+1}.

6.4 Cylindrical lens

A cylindrical lens focuses light into a line rather than a point. When creating a cylindrical metalens using supercells all the cells can be oriented the same way, which means that only polarization in one plane needs to be considered. This means that the dimensions of the first optimization, where only in-plane polarized light was studied, can be used. This can also be seen as a first step towards a spherical lens, which has a focus point. Since the supercell approach is not based on phase mapping, one needs to divide the lens into Frensnel zones in one direction, where each zone contains one deflection angle, which is then filled with the corresponding supercell, see Figure 6.6.

As discussed previous, the supercell was not optimized for deflection angles smaller than 31°, which would fill up the Fresnel zone in the middle of the lens. As mentioned, previous work has combined the supercell and dynamic phase approach when creating a lens, creating a zone in the middle of the lens where dynamic phase meta-atoms are used. It would be interesting try that for this metasurface as well, however the optimization of that type of meta-atom was not covered in this work. Instead, by making the lens deflecting light, the middle zone is not needed and instead a cutout was done, marked with a dashed circle in Figure 6.6. SEM images of a cylindrical lens can be seen in Figure 6.7, which shows, again, that the fabricated holes are smaller than the designed holes and that they have some roughness around the edges. In Figure 6.8, simulated and measured Fourier plane of a cylindrical lens deflecting with 61° can be seen. The measurement shows an oval dot placed on the target angle. The simulation shows a spot that is slightly more elongated in the Fourier plane which corresponds to a more focused beam spot than was measured. This is probably due to fabrication limitations and that the simulation was

done using a perfect Gaussian beam and deflecting lens. However some focusing was achieved with the fabricated metasurface. This can be seen in Figure 6.9 and 6.10, which shows the integrated cross section in k_x- and k_y-direction respectively, from characterization of cylindrical lenses with deflection angles 61° and 65°. As visualized in the inset of both figures, the beam waist in the Fourier plane is in k_y-direction almost half ($w/2$) the value of the waist in k_x-direction (w). Hence the focus is stronger in the k_x-direction which should be the case for a cylindrical lens. Looking at the propagating beam in real space in Figure 6.11 some focusing can be seen since the beam becomes more narrow. However the focus is not as tight as desired, the smallest diameter seems to be around 15 μm. A possible explanation to why the focus is not as good as designed could be that the discretization of the angles (steps of 1°) and thus the Fresnel zones, is too rough. This could, especially for larger angles where the corresponding Frensel zones are greater, give rise to many parallel rather than focusing rays. A solution could be to include more supercells with finer discretization, or to make an interpolation between the already obtained simulations and based on that make a smaller step size. Another possible explaination could be that the size of the beam that was used in the measurement set-up was to small, meaning that the whole metasurface was not illuminated. Larger deflection angels, which are placed at the edge of the metalens, will therefore not be utilized which in turn makes the numerical aperture lower, see Figure 3.2.

Nevertheless, the measured relative transmission (η) for the cylindrical lenses were 96.2% for 61° and 93.6% for 65°. Due to the limitation in numerical aperture used in measurements, cylindrical lenses with higher deflection angels could not be measured and were therefor not fabricated. However, based on the simulation and well corresponding measurements of the actually fabricated metasurfaces, it is believed that lenses with higher deflection angles could be fabricated successfully.

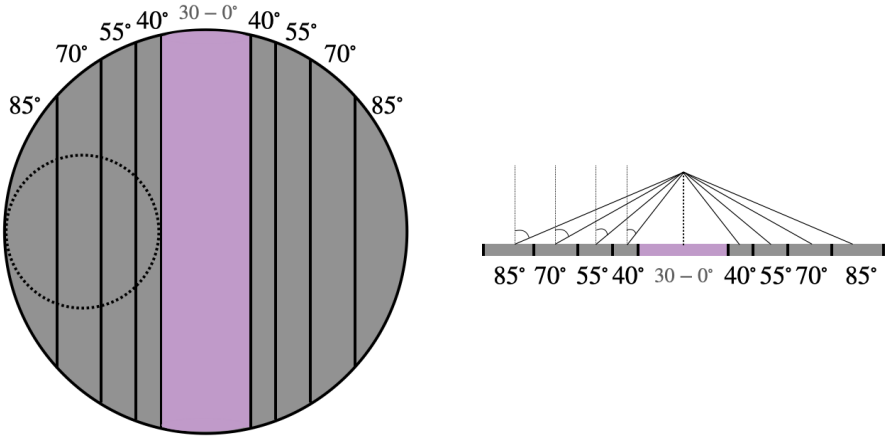

Figure 6.6: Sketch of cylindrical lens utilizing Fresnel zones. Each zone corresponds to a deflection angle with respect to the normal. On the left hand side is a sketch from above with a dashed circle showing a cutout that can be made to create a deflecting lens. The right hand side shows a sketch from the side.

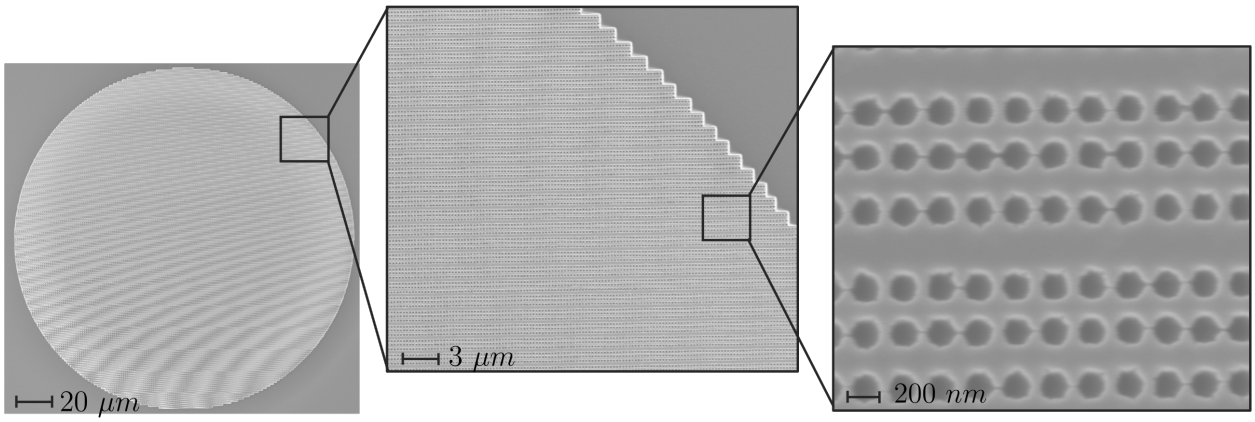

Figure 6.7: SEM images of a cylindrical lens metasurface. Different types of supercells are placed in the different zones but with same orientation.

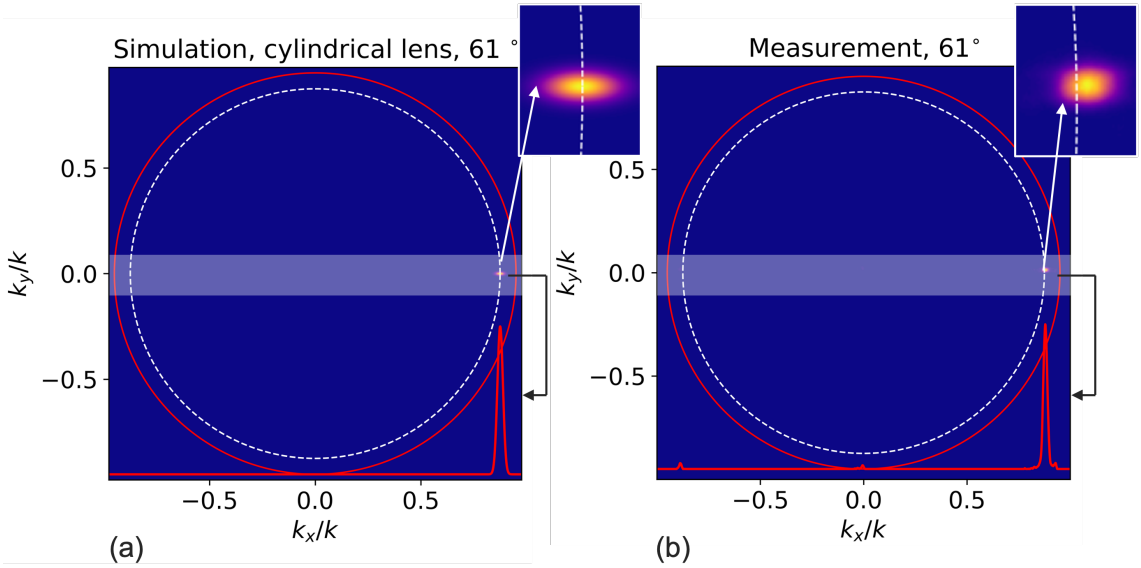

Figure 6.8: (a) Simulated and (b) measured Fourier images of a cylindrical metalens deflecting with 61°. The dashed white line marks the target angle, the red line the maximum collection angle. The red graph at the bottom shows the integrated intensity of the highlighted cross section, were the peaks from left to right corresponds to T_{-1}, T_0 and T_{+1}. The inset shows an in-zoomed image of the T_{+1} spot in the Fourier plane.

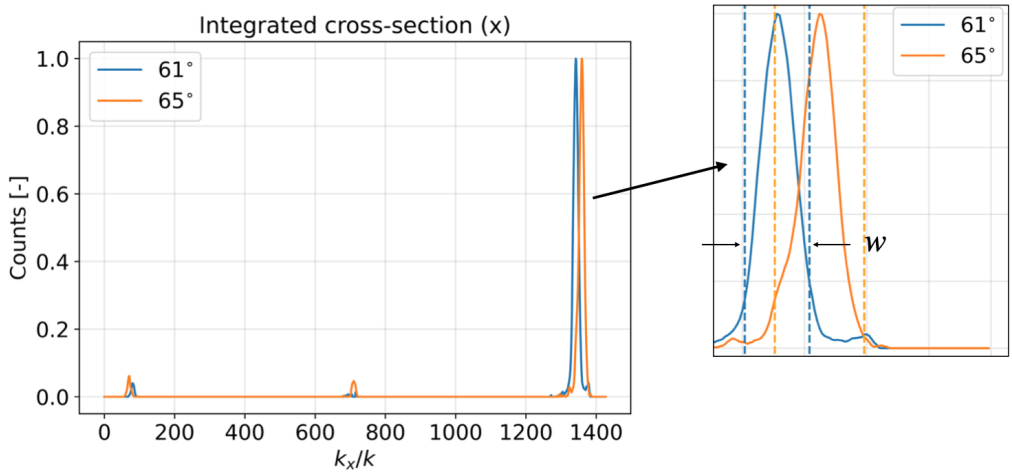

Figure 6.9: Integrated cross-section i k_x-direction of the measured Fourier plane for cylindrical metalenses with deflection angles 61° and 65°. The peak to the left corresponds to transmission order T_{-1}, the middle one is T_0 and the one to the right is T_{+1}. In the inset, dashed lines can be seen which marks the width, w, at the intensity value $1/e^2$ of the T_{+1}-peak.

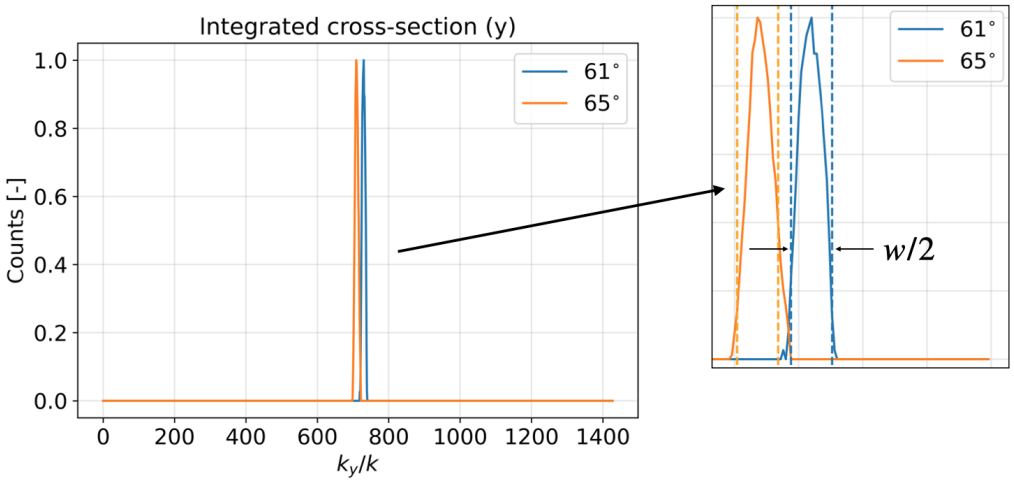

Figure 6.10: Integrated cross-section i k_y-direction of the measured Fourier plane for cylindrical metalenses with deflection angles 61° and 65°. The peak to the left corresponds to transmission order T_{-1}, the middle one is T_0 and the one to the right is T_{+1}. In the inset, dashed lines can be seen which marks the width, $w/2$, at the intensity value $1/e^2$ of the T_{+1}-peak.

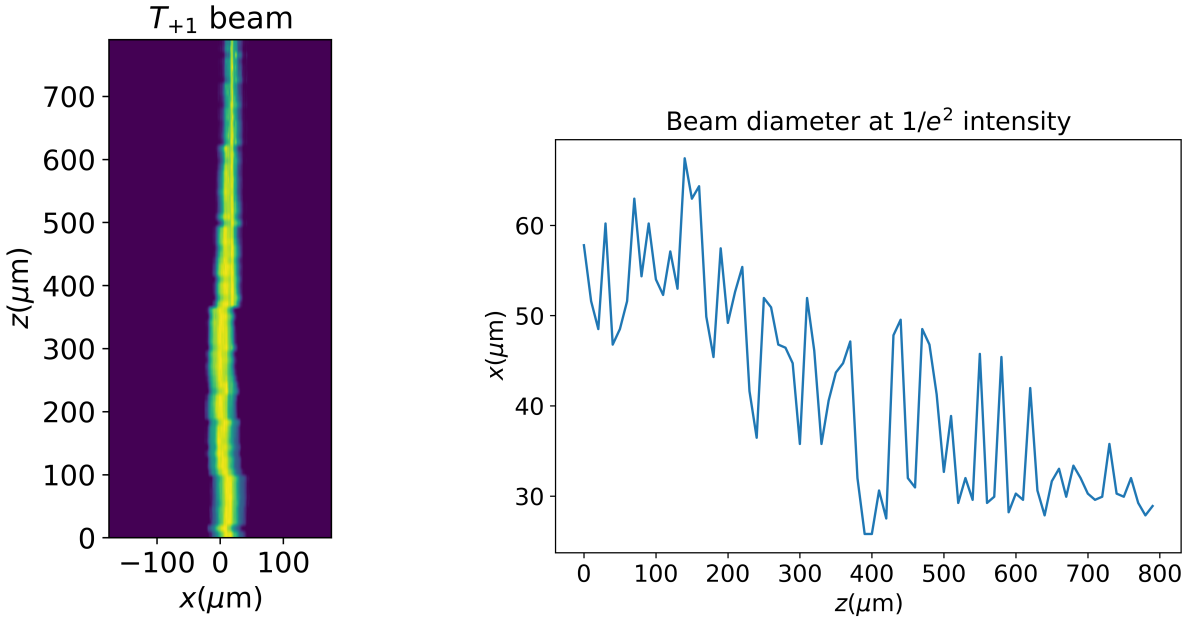

(a) **(b)**

Figure 6.11: Real space measurement of a cylindrical lens deflecting with 61°, (a) shows a z-stack image that was done taking pictures in steps of 10 μm, always keeping the T_{+1} beam in the center of the picture (b) shows the beam diameter at the intensity $1/e^2$.

6.5 Spherical lens

As stated previously, spherical lenses focus light into one point. Compared to the cylindrical lens, the Fresnel zones are rings, which depending on the radius of the lens, are filled with supercells corresponding to that deflection angle, see Figure 6.12. Using supercells, it means that the cells have to rotate around the lens, since the deflected light should always point to the center. However, which was also introduced earlier, the VCSEL emits linearly polarized light in one plane, which means that the rotation of the supercell makes a difference. For instance, if the supercell, positioned at zero degrees on a unit circle, is exited with in-plane polarized light, it means that it will be exited with out-of-plane polarized light, positioned at 90 degrees of the unit circle. Hence the design of the supercell needs to be optimized for both in-plane and out-of-plane polarized light. This was done, as the second optimization discussed in the Simulation section.

Moreover, for angles smaller than 31°, which would constitute the inner Fresnel zones of the lens, a dynamic phase metasurface could be used. Again, that is not covered in this work and instead lenses with deflected focal points were made, by making a cutout in the lens, which is visualized by the dashed circle in Figure 6.12. When creating the pattern for the cutout in the spherical lens the curvature was shown to be rather flat meaning that the rotation of supercells was small. There-

for the dimensions from simulations using only in-plane polarized light, due to its higher relative and total transmission, were used. Figure 6.13 shows SEM images of a fabricated spherical metalens, in which it can be seen that the radius of the fabricated holes are smaller than the designed radius, and also that there is some roughness around the edges. The simulated values for both in-plane and out-of-plane will however be needed if a non-deflecting lens is fabricated. In Figure 6.14 the Fourier plane for a simulated and measured spherical metalens, deflecting with 61°, can be seen. Again, the desired deflection angle is achieved, and a circular spot comparable with the size of the simulation can be seen. Figure 6.15 shows the integrated cross section of spherical lenses with deflecting angles 61° and 65° which have a relative transmission (η) of 95.5% and 93.8%, respectively. Comparing with Figure 6.5, which shows the integrated cross section for metalenses using only one type of supercell, the Fourier plane beam waist is broader. This would suggest a more focused beam compared to the unfocused plane waves in Figure 6.5. Still, studying the beam propagation in real space in Figure 6.16, the focusing effect does not seem to be as high as desired. As for the cylindrical lens, this could be a result of parallel rather than focusing rays due to rough discretization or the used beam being too narrow, which does not properly illuminate the metasurface.

As for the cylindrical lens, the spherical lens was not fabricated for deflection angels larger than 65° due to measurement limitations. Again, functional spherical lenses with greater deflection angles are supported by both simulation and fabrication of other angles.

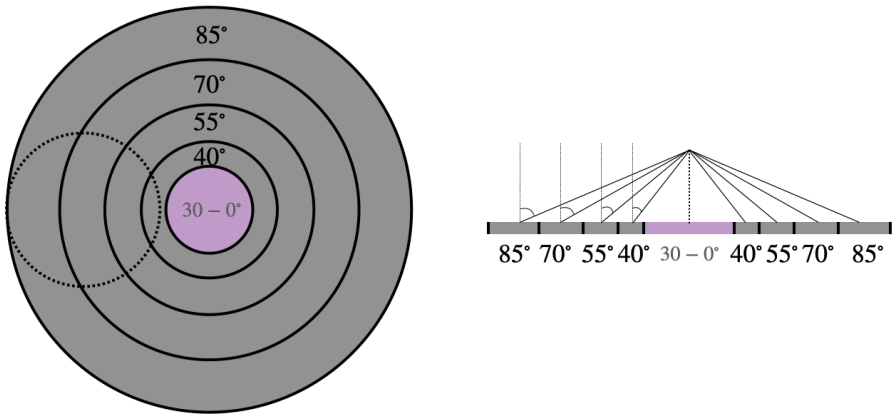

Figure 6.12: Sketch of spherical lens utilizing Fresnel zones. Each zone corresponds to a deflection angle with respect to the normal. On the left hand side is a sketch from above with a dashed circle showing a cutout that can be made to create a deflecting lens. The right hand side shows a sketch from the side.

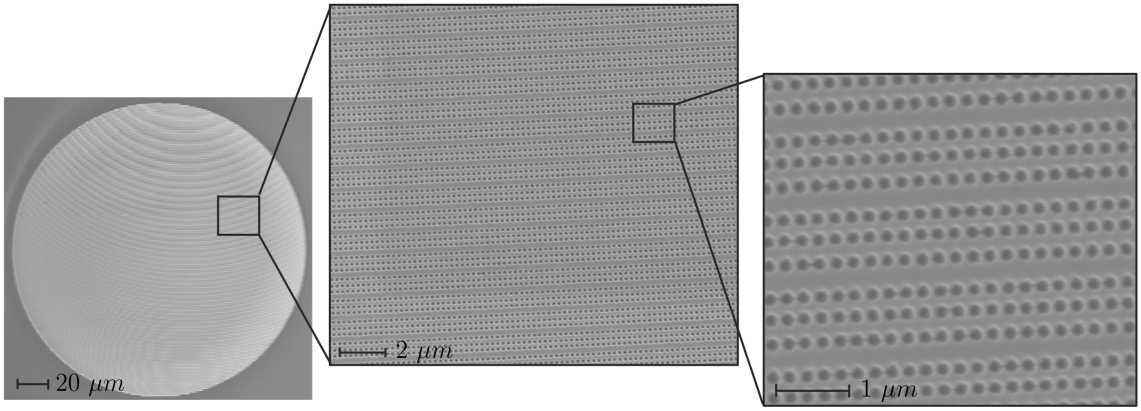

Figure 6.13: SEM images of a spherical lens metasurface. Different types of supercells are placed in the different zones and with different orientation, creating the visible curvature.

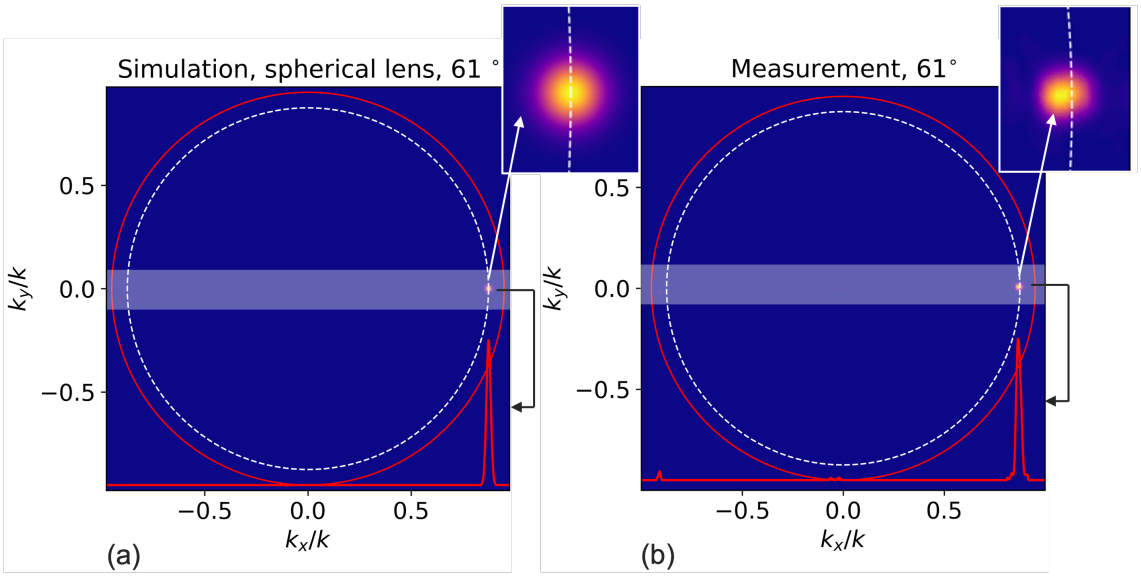

Figure 6.14: (a) Simulated and (b) measured Fourier images of a spherical metalens deflecting with 61°. The dashed white line marks the target angle, the red line the maximum collection angle. The red graph at the bottom shows the integrated intensity of the highlighted cross section, were the peaks from left to right corresponds to T_{-1}, T_0 and T_{+1}. The inset shows an in-zoomed image of the T_{+1} spot in the Fourier plane.

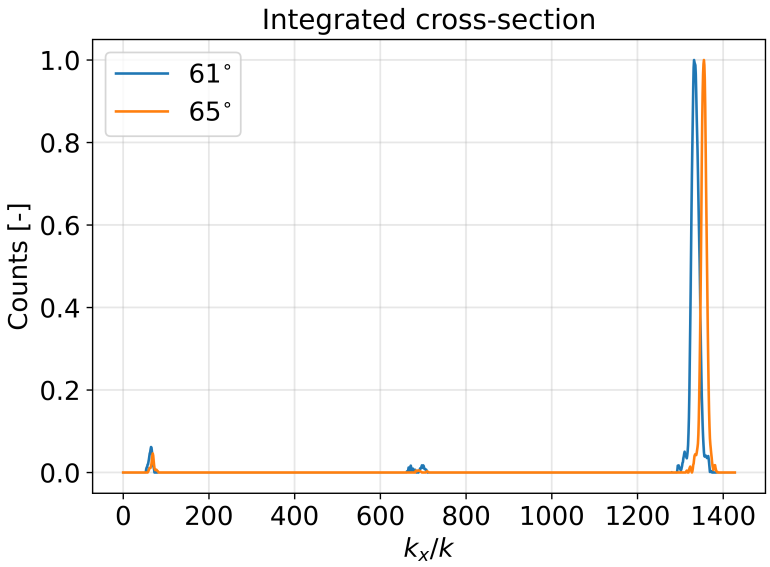

Figure 6.15: Integrated cross-section of the measured Fourier plane for spherical metalenses with deflection angles 61° and 65°. The peak to the left corresponds to transmission order T_{-1}, the middle one is T_0 and the one to the right is T_{+1}.

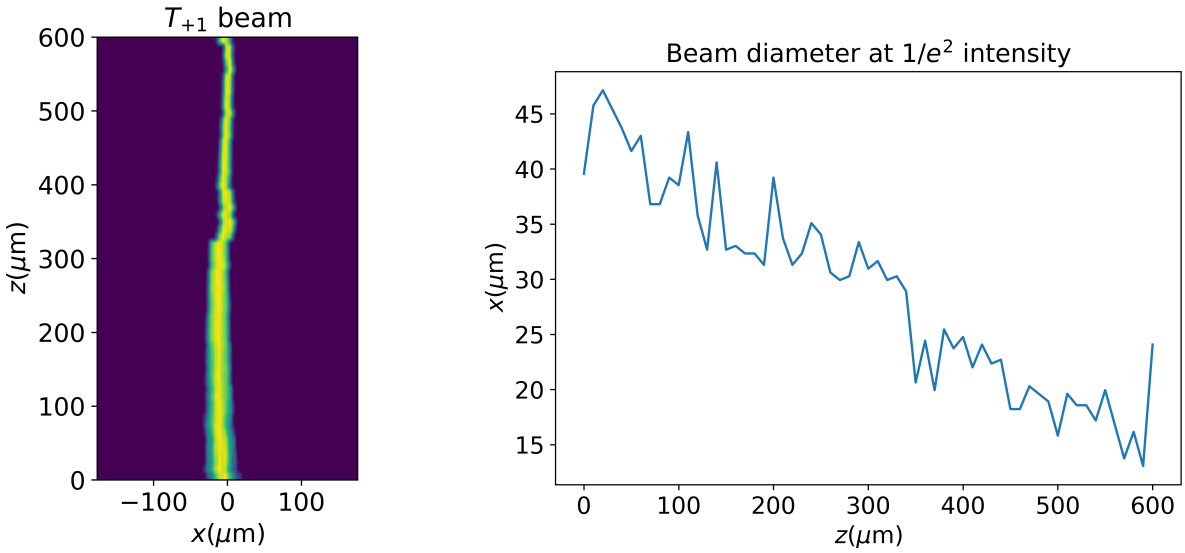

(a) **(b)**

Figure 6.16: Real space measurement of a spherical lens deflecting with 61°, (a) shows a z-stack image that was done taking pictures in steps of 10 μm, always keeping the T_{+1} beam in the center of the picture (b) shows the beam diameter at the intensity $1/e^2$.

7
Conclusions

In this project metasurfaces that can be integrated with GaAs VCSELs have been simulated, fabricated and characterized. The goal of the project was to deflect and focus light with a large deflection angle. The supercell metasurface approach was used, which is based on diffraction, where the size of the period of the supercell sets the deflection angle. Each supercell contained nano-holes, which were used to successfully circumvent the issue of aspect ratio dependent etching.

The simulations were done in two steps. First for incident light with in-plane polarization. The simulations showed high total and relative transmission for the desired diffraction order. Based on the simulations, three types of metasurfaces were fabricated. The first one contained only one type of supercell corresponding to one deflection angle which showed quite good agreement with simulations. Differences are assigned to fabrication defects, like smaller fabricated hole radius compared to the pattern radius and also rough edges of the holes. Further it was hard to get the exact same height of the holes as in simulations. The second type was a deflecting cylindrical lens, which from Fourier plane measurements shows good agreement with the target deflection angle and a focusing effect in one direction. However real space measurements do not show a very focused beam. The third type was a deflecting spherical lens. Again the desired deflection angle was achieved and focus in two directions could be seen in the Fourier plane, but not in real space. For both the cylindrical and spherical lens, the focus issue could be due to creation of many parallel, rather than focusing, rays. This in turn could be due to a too rough discretization of the angles and Fresnel zones of the lenses. Another possible explanation could be that the laser beam in the used measurement set-up was too narrow.

The other simulation was optimized for both in-plane and out-of-plane polarized light. This was done to be able to create a spherical lens for light emitted from VCSELs which is linearly polarized in one direction. The simulated transmission tended to be lower than for the previous simulation, both for in-plane and out-of-plane. Moreover there was a difference in transmission between the two polarization directions, so the geometry might not be the most suitable for this configuration. However when creating a deflecting spherical lens the cut out curvature was rather flat why the optimization for only in-plane polarized light was used in fabrication. Nevertheless, the optimized values for both in-plane and out-of-plane could be used for a non-deflecting spherical lens.

To create lenses with better focus, an idea would be to refine the discreization of the

lenses by either do more simulations or interpolate between the already simulated angels. Another improvement would be to modify the measurement set-up to be able to properly illuminate all the supercells in the metasurfaces. As a fist step towards the bigger goal of optical tweezing, it would be very interesting to trap a particle in a microfluidic channel, using the simulated and fabricated deflecting spherical metalenses, with an external laser. Then as a next step, the same experiment but instead integrating the metasurface with a VCSEL, should be carried out to see if it is possible to trap something using metasurface integrated VCSELs. Further, it could be a good idea to try other optimization algorithms to see if better results can be obtained for the simulation of in-plane and out-of-plane polarized light. Another thing to investigate would be angles smaller than 31° to make a complete lens, for instance using the dynamic phase metasurface and some kind of relation between the radius and height of the holes to still account for ARDE.

Bibliography

[1] A. Larsson, *Semiconductor Optoelectronics - Device Physics and Technologies*. Chalmers University of Technology, 2015.

[2] M. Juodėnas, E. Strandberg, A. Grabowski, *et al.*, "High-angle deflection of metagrating-integrated laser emission for high-contrast microscopy," *Light: Science Applications*, vol. 12, pp. 2047–7538, 2023. DOI: https://doi.org/10.1038/s41377-023-01286-0.

[3] Y.-Y. Xie, P.-N. Ni, Q.-H. Wang, *et al.*, "Metasurface-integrated vertical cavity surface-emitting lasers for programmable directional lasing emissions," *Nature nanotechnology*, vol. 15, pp. 125–130, 2020. DOI: https://doi.org/10.1038/s41565-019-0611-y.

[4] D. Wen and K. B. Crozier, "Semiconductor lasers with integrated metasurfaces for direct output beam modulation, enabled by innovative fabrication methods," *Nanophotonics*, vol. 12, pp. 1443–1457, 2023. DOI: https://doi.org/10.1515/nanoph-2022-0585.

[5] K. C. Neuman and S. M. Block, "Optical trapping," *Rev. Sci. Instrum.*, vol. 75, pp. 2787–2809, 2004. DOI: https://doi.org/10.1063/1.1785844.

[6] A. Kroner, "Vcsel-based optical trapping systems for microfluidic applications," vol. 0, p. 164, 2011.

[7] R. A. Flynna, A. L. Birkbecka, M. Grossa, *et al.*, "Parallel transport of biological cells using individually addressable vcsel arrays as optical tweezers," *Sensors and Actuators B: Chemical*, vol. 87, pp. 239–243, 2002. DOI: https://doi.org/10.1016/S0925-4005(02)00242-3.

[8] Y. Ogura, K. Kagawa, and J. Tanida, "Optical manipulation of microscopic objects by means of vertical-cavity surface-emitting laser array sources," *Applied Optics*, vol. 40, pp. 5430–5435, 2001. DOI: https://doi.org/10.1364/ao.40.005430.

[9] R. Michalzik, A. Kroner, A. Bergmann, and F. Rinaldi, "Vcsel-based optical trapping for microparticle manipulation," *Proc. SPIE 7229*, 2009. DOI: https://doi.org/10.1117/12.810154.

[10] A. Bergmann, N. I. Khan, J. A. M. Calahorro, D. Wahl, and R. Michalzik, "Hybrid integration approach of vcses for miniaturized optival defelction of mircoparticles," *Proc. SPIE 8432*, 2012. DOI: https://doi.org/10.1117/12.922610.

[11] M. B. Sanayeh, A. Bergmann, and R. Michalzik, "Simultaneous optical manipulation of multiple particles inside microfluidix channels using one rectangular-shaped vcsel," *Proc. SPIE 9129*, 2014. DOI: https://doi.org/10.1117/12.2051610.

[12] J. Xiao, T. Plaskocinski, M. Biabanifard, S. Persheyev, and A. D. Falco, "On-chip optical trapping with high na metasurfaces," *ACS Photonics*, vol. 10, pp. 1341–1348, 2023. DOI: https://doi.org/10.1021/acsphotonics.2c01986.

[13] N. Yu and F. Capasso, "Flat optics with designer metasurfaces," *Nature materials*, vol. 13, pp. 139–150, 2014. DOI: https://doi.org/10.1038/nmat3839.

[14] N. Yu, P. Genevet, M. A. Kats, *et al.*, "Light propagation with phase discontinuities: Generalized laws of reflection and refraction," *Science*, vol. 334, pp. 333–337, 2011. DOI: https://doi.org/10.1126/science.1210713.

[15] M. Kang, Y. Ra'di, D. Farfan, and A. Alù, "Efficient focusing with large numerical aperture using a hybrid metalens," *American Physical Society*, vol. 13, p. 044 016, 2020. DOI: https://doi.org/10.1103/PhysRevApplied.13.044016.

[16] Y. Ra'di, D. L. Sounas, and A. Alù, "Metagratings: Beyond the limits of graded metasurfaces for wave front control," *Physical Review Letters*, vol. 119, p. 067 404, 2017. DOI: https://doi.org/10.1103/PhysRevLett.119.067404.

[17] R. Paniagua-Dominguez, Y. F. Yu, E. Khaidarov, *et al.*, "A metalens with a near-unity numperical aperture," *Nano letters*, vol. 18, pp. 2124–2132, 2018. DOI: https://doi.org/10.1021/acs.nanolett.8b00368.

[18] M. Hentschel, K. Koshelev, F. Sterl, *et al.*, "Dielectric mie voids: Confining light in air," *Light: Science Applications*, vol. 12, 2023. DOI: https://doi.org/10.1038/s41377-022-01015-z.

[19] D. Conteduca, I. Barth, G. Pitruzzello, C. P. Reardon, E. R. Martins, and T. F. Krauss, "Dielectric nanohole array metasurface for high-resolution near-field sensing and imaging," *Nature Communication*, vol. 12, 2021. DOI: https://doi.org/10.1038/s41467-021-23357-9.

[20] T. Rylander, A. Bondeson, and P. Ingelström, *Computational Electromagnetics*. Springer, 2013.

[21] F. W. Low, C. W. Lai, N. A. Samsudin, *et al.*, "Chapter 5 - graphene and its derivatives, synthesis route, and mechanism for photovoltaic solar cell applications," in *Sustainable Materials for Next Generation Energy Devices*, K. Y. Cheong and L.-C. Chen, Eds., Elsevier, 2021, pp. 103–132. DOI: https://doi.org/10.1016/B978-0-12-820628-7.00005-8. [Online]. Available: https://www.sciencedirect.com/science/article/pii/B9780128206287000058.

[22] N. Hardy, "What is reactive sputtering?," 2013. [Online]. Available: https://www.semicore.com/news/67-reactive-sputtering-basics.

A

Simulation model and results

A.1 Validation of simulation model

To verify that the models used for the simulations were correct, convergence studies were carried out for the parameters c_{mesh}, h_{sub}, h_{air} were made. A parametric sweep was done for each and the simulated solutions were extrapolated to find the zero cell size [20]. This was done by doing a curve fit to a power series according to equation A.1 and then look at the difference between the simulated data and the curve fit to get the error, see equation A.2.

$$f(x) = f_0 + f_1 x^{\alpha} \tag{A.1}$$

$$e(x) = \left| \frac{Q - f_0}{Q} \right| \tag{A.2}$$

In the equations above Q is the simulated quantity (e.g. Transmission), x is the parameter under investigation (e.g. c_{mesh}), f_0 is the value of the function f when the parameter value goes to infinity ($f(x \to \infty) = f_0$), f_1 is a constant, α is the convergence rate.

A.1.1 Mesh study

Starting with c_{mesh}, which is a parameter that sets the size of the mesh according to equation A.3, where l_{max} is the maximum element size in a domain, λ_0 is the vacuum wavelength and n is the refractive index.

$$l_{max} = \frac{\lambda_0}{n c_{mesh}} \tag{A.3}$$

Figure A.1, shows the simulated data with a fitted curve and the error function for c_{mesh}. As can be seen in the figure, the function converges for $c_{mesh} > 6$ and therefore $c_{mesh} = 8$ was chosen.

A.1.2 Starting conditions

For the starting condition, convergence studies of h_{air} and h_{sub} was made. Figure A.2 and A.3 shows simulated data with fitted curves and error functions. As can be seen in the figures (A.2 and A.3), the transmission oscillates and does not seem to converge, however the oscillations are small and only give a factor of 10^{-3} in error.

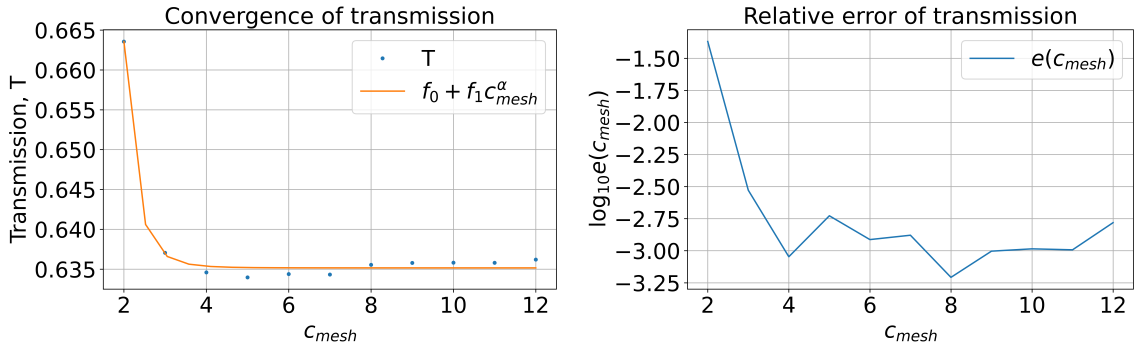

(a) **(b)**

Figure A.1: Convergence study for the mesh (c_{mesh}) measuring transmission (T). (a) shows the data with fitted curve and (b) the estimated error.

However, to be sure that that the field is absorbed, $h_{air} = 2000$ nm and $h_{air} = 1000$ nm was chosen for the simulations.

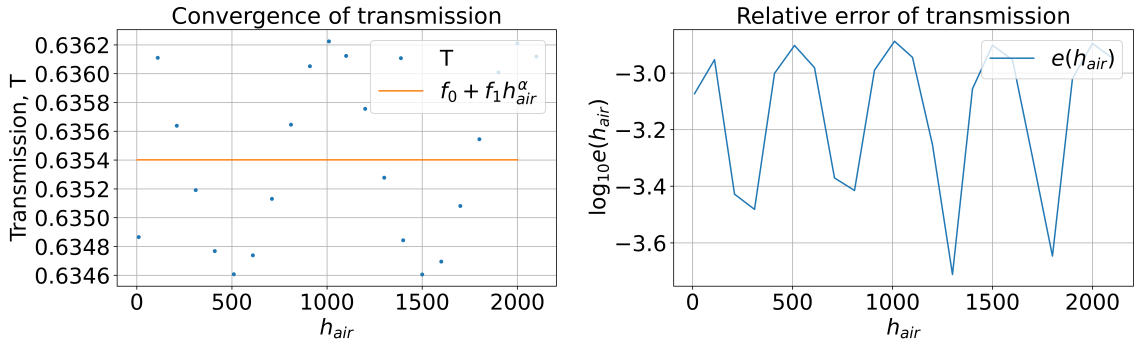

(a) **(b)**

Figure A.2: Convergence study for placement of the top port (h_{air}) measuring transmission (T). (a) shows the data with fitted curve and (b) the estimated error.

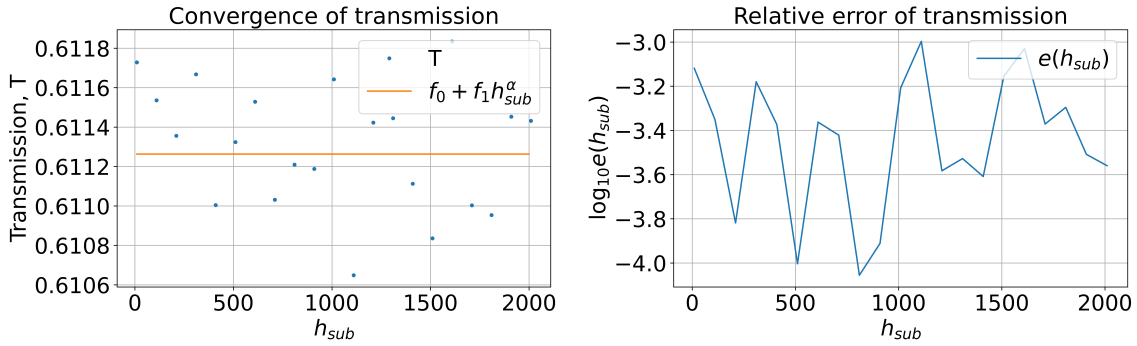

(a) **(b)**

Figure A.3: Convergence study for placement of the bottom port (h_{sub}) measuring transmission (T). (a) shows the data with fitted curve and (b) the estimated error.

A.1.3 PLM truncation

For the supercell model, $h_{pml} = 400$ nm is used, both for the PML below the GaAs substrate and the PML above the block of air. The decay of the E-field in the top PML can be seen in Figure A.4, where a drop of almost 2.5 orders of magnitude over the PML, can be seen.

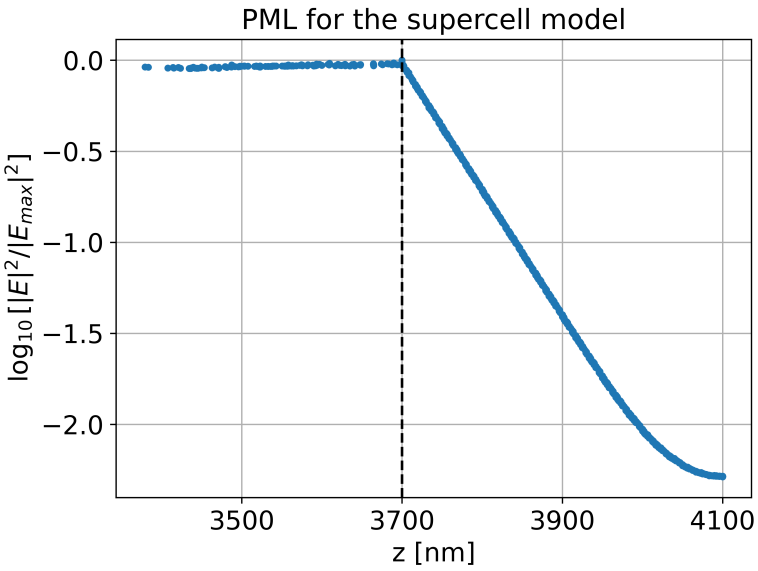

Figure A.4: The electric field through the PML at the top of the supercell. The black dahsed line shows where the top PML starts.

A.2 Optimization supercell

Optimized dimensions for the supercell for deflecting angles between 85° and 31° can be seen in table A.1 for in-plane polarized light and in table A.2 for in-plane and out-of-plane polarized light.

Table A.1: Optimized dimensions for deflection angles between 85° and 31°, considering in-plane linearly polarized light. For all angles, $P_{nd} = 240$ nm, $r = 110$ nm and $h_{meta} = 700$ nm were used. The definitions of the parameters Figure 4.1.

Angle (°)	P_d [nm]	g_1 [nm]	g_2 [nm]	g_3 [nm]	g_4 [nm]	η (T_{+1})	T_{tot}
85	988	93	492	766		0,825187924	0,70255
84	989	92	492	767		0,812989267	0,68099
83	991	91	490	768		0,798967398	0,66202
82	994	95	495	773		0,810912387	0,67849
81	996	96	497	775		0,81860331	0,71137
80	999	98	498	776		0,841835658	0,75822
79	1002	100	501	779		0,856557897	0,80396
78	1006	101	503	781		0,874310873	0,83765
77	1010	98	502	780		0,884775654	0,84713
76	1014	105	510	789		0,889973058	0,84181
75	1019	110	527	798		0,899139548	0,83049
74	1024	106	525	799		0,898220995	0,81894
73	1029	106	534	803		0,899938273	0,79868
72	1035	106	532	807		0,90936221	0,78745
71	1041	115	534	819		0,913297146	0,78757
70	1047	110	545	823		0,912186997	0,76725
69	1054	116	543	830		0,925192041	0,76534
68	1061	110	557	837		0,87761796	0,75341
67	1069	118	556	846		0,929431981	0,73941
66	1077	106	566	848		0,871858295	0,7417
65	1086	102	569	852		0,926842503	0,69806
64	1095	117	581	873		0,914126384	0,71392
63	1104	113	592	878		0,89975824	0,67836
62	1115	107	596	879		0,908703032	0,66422
61	1125	136	609	904		0,961974936	0,61155
60	1136	108	596	895		0,919204065	0,66771
59	1148	94	586	891		0,902609639	0,67206
58	1160	91	593	900		0,877243935	0,68691
57	1173	75	594	899		0,845038424	0,70867
56	1187	69	599	906		0,833958426	0,72656
55	1201	75	589	908		0,908144853	0,65938
54	1216	66	616	923		0,899925498	0,72495
53	1232	75	621	941		0,895519975	0,71742
52	1249	67	623	946		0,897996677	0,71654
51	1266	60	627	952		0,902468824	0,70094
50	1285	30	611	938		0,904480758	0,6829
49	1304	25	618	949		0,899967837	0,67839
48	1324	23	627	961		0,911035319	0,66604
47	1345	12	628	965		0,916243777	0,65689
46	1368	7	628	964		0,943444057	0,60355

Angle (°)	P_d [nm]	g_1 [nm]	g_2 [nm]	g_3 [nm]	g_4 [nm]	η (T_{+1})	T_{tot}
45	1392	11	626	961		0,873966255	0,55332
44	1417	2	640	985		0,92384029	0,50103
43	1443	3	650	997		0,910959735	0,49472
42	1471	3	660	1009		0,912527256	0,48016
41	1500	2	680	1037		0,913	0,41884
40	1530	2	692	1039		0,909627528	0,33916
39	1564	2	710	1063		0,86636814	0,34882
38	1598	2	720	1082		0,800521201	0,3515
37	1635	2	729	1096		0,728142033	0,34657
36	1674	2	328	680	900	0,695558377	0,52379
35	1716	2	328	680	900	0,716804478	0,52378
34	1760	7	328	680	904	0,702684985	0,46678
33	1807	4	328	680	900	0,65707954	0,52118
32	1857	4	330	680	900	0,613887016	0,5385
31	1911	4	330	680	900	0,620097606	0,56554

Table A.2: Optimized dimensions for deflection angles between 85° and 31°, considering in-plane (ip) and out-of-plane (op) linearly polarized light. For all angles, P_{nd} = 240 nm, r = 110 nm and h_{meta} = 700 nm were used. The definitions of the parameters can be seen in Figure 4.1.

Angle (°)	P_d	g_1	g_2	g_3	g_4	η (T_{+1}, ip)	T_{tot} (ip)	η (T_{+1}, op)	T_{tot} (op)
85	988	92	492	765		0,827949	0,69973	0,439117	0,10618
84	989	91	491	766		0,813093	0,68093	0,495142	0,12248
83	991	89	490	765		0,815424	0,64753	0,617921	0,17758
82	994	94	495	771		0,823117	0,66698	0,695002	0,26546
81	996	94	497	77		0,825962	0,70273	0,729557	0,29387
80	999	99	500	776		0,852723	0,74688	0,712359	0,31479
79	1002	96	497	773		0,869375	0,7907	0,694942	0,31224
78	1006	101	503	779		0,884902	0,82635	0,678672	0,30907
77	1010	103	502	778		0,886092	0,82826	0,665853	0,35006
76	1014	99	502	779		0,895905	0,82942	0,67397	0,35117
75	1019	108	515	793		0,900958	0,81883	0,698521	0,35641
74	1024	91	503	782		0,902941	0,80948	0,71359	0,36027
73	1029	105	522	801		0,900044	0,79832	0,755958	0,35555
72	1035	99	522	802		0,897299	0,7916	0,779405	0,36496
71	1041	103	533	813		0,883594	0,78352	0,812394	0,36801
70	1047	94	530	812		0,854536	0,78475	0,799506	0,39078
69	1054	114	546	829		0,923308	0,76021	0,755986	0,30718
68	1061	115	553	836		0,9241	0,74682	0,77533	0,31633
67	1069	112	557	840		0,923382	0,73151	0,794997	0,32443
66	1077	110	562	846		0,92242	0,72107	0,800065	0,33262
65	1086	102	564	849		0,909976	0,71986	0,919356	0,33629
64	1095	110	579	866		0,91366	0,70746	0,79638	0,34527
63	1104	110	586	876		0,900955	0,69366	0,762208	0,35688
62	1115	112	597	885		0,892201	0,67797	0,82818	0,33697
61	1125	103	592	884		0,896921	0,6821	0,783538	0,33764
60	1136	101	594	893		0,871727	0,69949	0,664992	0,34196
59	1148	60	587	870		0,747022	0,72614	0,890842	0,31842
58	1160	57	593	877		0,744812	0,73631	0,877803	0,34786
57	1173	48	596	881		0,721868	0,75484	0,861271	0,38577
56	1187	69	621	909		0,776613	0,72784	0,839415	0,3853
55	1201	30	591	882		0,737861	0,72166	0,798346	0,42204
54	1216	46	617	910		0,791392	0,70764	0,776615	0,4583
53	1232	40	618	918		0,811063	0,70626	0,693554	0,47311
52	1249	41	624	932		0,840255	0,70162	0,599137	0,4866
51	1266	64	641	957		0,923601	0,66447	0,496714	0,48489
50	1285	36	624	945		0,91886	0,65971	0,49951	0,48051
49	1304	28	628	955		0,905171	0,66796	0,508352	0,47738
48	1324	31	645	975		0,907192	0,66028	0,451823	0,44348
47	1345	17	645	977		0,920067	0,64471	0,463024	0,43539
46	1368	3	650	977		0,944537	0,58083	0,517175	0,39746

Angle (°)	P_d	g_1	g_2	g_3	g_4	η (T_{+1}, ip)	T_{tot} (ip)	η (T_{+1}, op)	T_{tot} (op)
45	1392	7	636	964		0,859104	0,54896	0,430209	0,38336
44	1417	2	660	999		0,943653	0,50581	0,406819	0,3591
43	1443	2	670	1009		0,934889	0,5106	0,420145	0,34811
42	1471	2	680	1028		0,943373	0,47905	0,367875	0,34382
41	1500	2	700	1050		0,927398	0,43512	0,370493	0,34208
40	1530	5	696	1038		0,883066	0,34659	0,350233	0,27791
39	1564	27	705	1053		0,754793	0,38157	0,404363	0,31537
38	1598	2	730	1086		0,83254	0,34249	0,310076	0,25979
37	1635	2	750	1107		0,792598	0,32959	0,376578	0,31133
36	1674	32	323	662	901	0,527653	0,43626	0,879864	0,51633
35	1716	7	326	675	917	0,63238	0,48181	0,654267	0,534
34	1760	11	321	670	911	0,61824	0,4562	0,645986	0,54206
33	1807	9	324	674	913	0,598298	0,47785	0,595425	0,54135
32	1857	19	321	662	900	0,521799	0,48602	0,749201	0,51769
31	1911	3	327	680	921	0,610517	0,52486	0,604793	0,51838

B

Fabrication

B.1 Clearence test

A clearence test for the e-beam resist ARP6200 was done to see the smallest electron dose that is needed for the e-beam. The depth measuremet was done using an ellipsometer and the results can be seen in Figure B.1. The test shows that the E-beam dose have to be at least $180 - 200 \mu C/cm^2$.

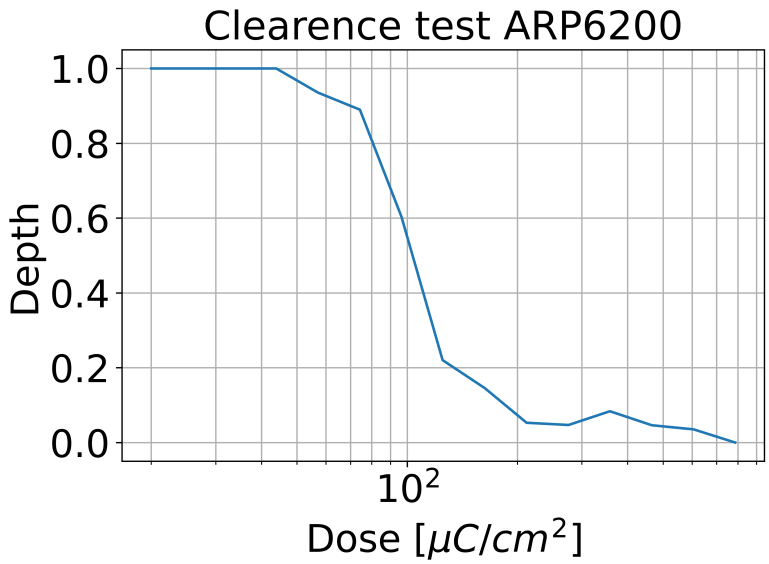

Figure B.1: Clearence test for the e-beam resist AR-P6200. Note that the depth values are normalized and that 1 means that no resist has been cleared.

DEPARTMENT OF MICROTECHNOLOGY AND NANOSCIENCE
CHALMERS UNIVERSITY OF TECHNOLOGY
Gothenburg, Sweden
www.chalmers.se

CHALMERS
UNIVERSITY OF TECHNOLOGY